JOURNAL OF GEOPHYSICAL RESEARCH, VOL. 98, NO. D5, PAGES 8639–8664, MAY 20, 1993

Measurements of High Number Densities of Ice Crystals in the Tops of Tropical Cumulonimbus

R. G. KNOLLENBERG

Particle Measuring Systems, Incorporated, Boulder, Colorado

K. KELLY

NOAA, Aeronomy Laboratory, Boulder, Colorado

J. C. WILSON

University of Denver, Denver, Colorado

Imaging and light scattering instruments were used during the January/February 1987 STEP Tropical Experiment at Darwin, Australia, to measure ice crystal size distributions in the tops of tropical cumulonimbus anvils associated with tropical cyclones and related cloud systems. Two light scattering instruments covered particles from 0.1-μm to 78-μm diameter. Particles larger than 50-μm diameter were imaged with a two-dimensional Grey optical array imaging probe. The measurements were made at altitudes ranging from 13 to 18 km at temperatures ranging from -60° to -90°C. Additional measurements made in continental cumulonimbus anvils in the western United States offer a comparative data set. The tropical anvil penetrations revealed surprisingly high concentrations of ice crystals. Number densities were typically greater than 10 cm^{-3} with up to 100 cm^{-3} if one includes all particles larger than 0.1 μm and can approach condensation nuclei in total concentration. In order to explain the high number densities, ice crystal nucleation at altitude is proposed with the freezing of fairly concentrated solution droplets in equilibrium at low relative humidities. Any dilute liquid phase is hypothesized to be transitory with a vanishingly short lifetime and limited to cloud levels nearer -40°C. Homogeneous nucleation of ice involving H_2SO_4 nuclei is attractive in explaining the high number densities of small ice crystals observed near cloud top at temperatures below -60°C. The tropical size distributions were converted to mass using a spherical equivalent size, while the continental anvil data were treated as crystalline plates. Comparisons of the ice water contents integrated from the mass distributions with total water contents measured with NOAA Lyman-alpha instruments require bulk densities equivalent to solid ice for best agreement. Correlation between the two data sets for a number of flight passes was quite good and was further improved by subtraction of water vapor density values ranging between ice and water saturation. Ice water contents up to 0.07 g m^{-3} were observed in the tropical anvils with over 0.1 g m^{-3} in continental anvils. The size distributions in tropical anvils generally reveal mass modes at sizes of 20-40 μm. With rare exceptions, particles larger than 100 μm were not observed near the cloud tops. In continental cumulonimbus anvils, much larger plate crystals approaching 1 mm in size account for the majority of the ice water. Most of the ice crystal mass lofted to anvil altitudes falls to lower levels prior to evaporating. The anvils can experience strong radiational heating as well as cooling depending upon lower cloud cover, particle size distribution, and time of day.

1. Introduction

The Ames Research Center (ARC) Stratosphere-Troposphere Exchange Project (STEP) for NASA incorporates a contingent of state-of-the-art techniques to focus on the central question of "why the stratosphere is so dry" [*Russell et al.* this issue; *Danielsen,* this issue]. In addition to measurements of water vapor gradients, cloud top temperatures, and the tracing of air parcels, cloud particle characteristics play an important role. The clouds of certain importance are the tops of cumulonimbus towers and their associated cirriform anvils which bridge the tropopause. The cold tropical tropopause provides an effective water vapor trap limiting the moisture available to the stratosphere as long as the tropics are the primary region of tropopause cumulonimbus penetrations. Scientists and experiments associated with STEP primarily address the role of cumulonimbus clouds in the tropics. These studies emphasize stratospheric-tropospheric exchange and transport processes in the lower stratosphere by means of a comprehensive set of meteorological, trace gas, and aerosol measurements on the NASA U-2 and/or ER-2 aircraft. The exchange was studied in the tropics and extratropics to test different proposed mechanisms for irreversible transfers of tropospheric air into the stratosphere, including both cloud-free and cloud-dominated mechanisms. A series of flights above clouds, orthogonal to the major jets, were also made to examine quasi-horizontal transfers associated with tropopause folding or relatively rapid transfers from low to high latitudes occurring within the stratosphere itself [*Russell et al.*, this issue].

Darwin was selected as the operational site for the STEP Tropical Experiment measurements because of its proximity to the coldest observed cloud tops. Cold tropopause and cloud top temperatures are required by existing dehydration models. *Danielsen* [1982] describes a "dehydration engine" model in

Paper number 92JD02525.
0148-0227/93/92JD-02525$05.00

which overshooting cloud turrets collapse and mix with still ascending air, diverging to form a large anvil in the stratosphere and entraining warmer stratospheric air. Danielsen argues that tropopause penetration is unlikely if one only considers equilibrium predictions of maximum cloud top levels. Rather, he suggests that positive buoyancy forces accelerate parcels through the equilibrium levels resulting in a potentially mixed (stratospheric/tropospheric air) anvil above the equilibrium level. Danielsen's model is quite different from the "stratospheric fountain" model suggested by *Newell and Gould-Stewart* [1981]. The "stratospheric fountain" is described as a geographically limited area coincident with the main tropospheric sources of sufficient moist static energy (moist static energy of the air at 1000 mbar over Darwin is $\approx 3.5 \times 10^5$ J/Kg) to be convectively lifted to the tropical tropopause ($\approx$100 mbar). Temperatures at the tropopause are frequently below the threshold value of 190.7 K, which is required to produce water vapor mixing ratios of 3.5 ppmv (2.2 $\mu g/g^{-1}$) observed in the stratosphere. However, the minimum temperatures produced are below the tropopause and it is necessary to invoke radiational heating to elevate the "freeze-dried" air into the stratosphere. This hypothesis operates utilizing slow vertical ascents from zonal flows in which the growing ice crystals have sufficient size and thus terminal velocity to sediment out thus leaving ascending air saturated with respect to ice at the minimum cloud top temperature. The picture as posed by *Danielsen* [1982] is thus quite different since he asserts that rather than continuous the transfer to the stratosphere is discrete; dehydration feeds upon turbulent transport within a convectively destabilized cirrus anvil within the stratosphere which is radiatively heated beneath cloud base and radiatively cooled at cloud top. However, only anvils with high ice water contents and thus high emissivities (0.9 or greater) have tops sufficiently shielded from strong upward IR irradiance to radiatively cool [*Ackerman et al.*, 1988; *Stephens*, 1983].

Both of the above suggested processes may involve secondary radiative heating of desiccated air to raise the "freeze-dried" air to higher levels. *Danielsen* [1982] suggests that this may occur at the waning stages of the anvil's life cycle when the anvil becomes optically thin. Implicit in the success of any dehydration process is that the particle mass be sufficiently low to not rehydrate the "freeze-dried" air, yet of sufficient optical density to generate the required heating.

The Particle Measuring Systems, Incorporated, (PMS), Particle Size Spectrometer Experiment (PSSE) as part of STEP was designed to quantitatively characterize the particulate makeup of the cloud tops and played a major role during the cloud missions [*Russell et al.*, this issue]. To detail cloud microphysical and radiative properties and determine the fate of cumulonimbus exhausted ice crystals, particle size measurements were required over a large size range (0.1 to 2000 μm) encompassing submicron aerosol ice forming nuclei (IFN), cloud hydrometeors (largely small ice crystals), and precipitation size particles (large ice crystals). Three separate instruments were used covering sizes of approximately 0.1-3.0 μm, 2-100 μm, and 100-2500 μm.

Submicron aerosols have been found useful during past experiments in identifying stratospheric air and enabling estimates of entrainment [*Knollenberg et al.*, 1982]. Furthermore, these small particles with concentrations of 10-100 cm^{-3} serve as the nuclei reservoir (including IFN) for new cloud particle growth. At temperatures below about -40°C the freezing of droplets via the homogeneous nucleation mechanism is very rapid, although condensation on cloud condensation nuclei (CCN) is first thought to be required to generate a transient liquid phase [*Heymsfield and Sabin*, 1989; *Sassen and Dodd*, 1988]. Under such conditions, nucleation and growth of high ice crystal concentrations can be extremely rapid, and the formation of small ice crystals a few tens of microns in size occurs quite rapidly. Soluble aerosol particles (e.g., NH_4SO_4) are generally the preferred CCN and thus IFN. At higher altitudes, H_2SO_4 aerosol may also contribute. The small crystals formed, if of sufficient size, would be expected to dominate the scattering and absorption cross sections, thus controlling radiative exchange processes. They are also the dominant controlling factor in regulating the excess water vapor budget. This range of particles includes sizes from submicron to approximately 100 μm having concentrations of 1-10,000 L^{-1}.

The largest precipitation size particles for which we have direct concern include those of 100 μm and larger. These particles have recognizable shapes and generally dominate the mass whenever present. The larger terminal velocities associated with such particles allow for rapid vertical exchange of water mass. These particles were observed in concentrations of 10 to 100 L^{-1}.

This experimental work required an additional measurement capability to that which existed on the U-2. Prior to this work we had measurement capabilities for aerosol from 0.1 to 3.0 μm using an active scattering aerosol spectrometer probe (ASAS-X) and a two-dimensional Grey imaging probe for large precipitation-type particles greater than 40-μm size. The lack of measurement capability between 3 and 40 μm had to be rectified since the tops of tropical cumulonimbus anvils often concentrate ice crystal mass in this size range. To fill this gap, we modified the two-dimensional probe to include a light scattering spectrometer subrange with a nominal 2- to 100-μm size range. Because of limitations in mounting locations a standard light scattering spectrometer probe (model FSSP-100 manufactured by PMS) covering a 3- to 45-μm size range and often used in place of the two- dimensional probe [*Knollenberg and Huffman*, 1983] could not be flown simultaneously with the two-dimensional probe. A combined light scattering/imaging instrument had to be designed and fabricated to replace both the FSSP and the two-dimensional probe. Section 2 describes the instrument's capability in some detail as well as an overview of the PSSE.

2. Particle Size Spectrometer Experiment Instrument Descriptions

The preexisting PSSE that was used in the 1980 Panama experiments in cumulonimbus anvils was packaged to fit in the forward half of a U-2 wing tank pod. The two-dimensional and ASAS-X were adaptations of standard instruments manufactured by PMS for various field programs on aircraft. The data acquisition system (DAS) was necessarily custom designed for the U-2 to meet space constraints. The ASAS-X was packaged with the data acquisition system as a single integrated unit. A ground playback system was also assembled for postflight data editing.

For the STEP programs the PSSE was modified to combine the functions of the FSSP-100 instrument and the two-dimensional instrument. Including the aerosol probe, this allowed full spectral coverage of particles from 0.1 μm to several millimeters

in size. We made no changes in the ASAS-X or data acquisition system. A descriptive overview of the combined FSSP two-dimensional instrument follows. A more detailed optical description is provided in the Appendix. Since the ice mass is concentrated in the largest sizes and because the crystalline habit becomes more varied as size increases, it was highly desirable to measure all sizes greater than 2 μm by "in situ" methods and to fully image all particles possible. All measurements had to be made on a continuous basis without compromising the available 6 hours of on-board data storage of the DAS.

Besides the above issues the operating air speeds of the U-2/ER-2 (nominal 200 m s^{-1}) raise the nominal minimum detectable particle sizes for both the standard two-dimensional and the FSSP-type instruments by about a factor of 2. Because of the overall greater complexity of the two-dimensional versus the FSSP it was desirable to leave as much of the two-dimensional electronics as standard as possible. The decision was made to start with a two-dimensional probe rather than an FSSP-100, keep the bulk of the two-dimensional hardware intact, and adapt the FSSP to operate "piggy-back." The two-dimensional electronics were essentially unmodified. The two-dimensional optical system was allocated 80% of the available light and the FSSP optical system 20% of the available light of the single laser available. Because the illuminating laser beam cross section dictated by the two-dimensional was large (4 X 0.5 mm), the FSSP was required to use a nonstandard sample volume definition scheme. In essence, a small portion of the transmitted beam and scattered light signals were separated from the two-dimensional imaging optics train and sensed with preamps, the signals of which were transmitted to the DAS for pulse height analysis (PHA) for particle sizing and sample volume definition.

There was only space for a single laser, and it was necessary to isolate separate sections of the exposed laser beam (via separation of viewing angles) to perform the individual light scattering and imaging measurements. The open mechanical sample aperture dictated by the two-dimensional imaging requirements is much wider than in a standard FSSP resulting in a reduction of the FSSP collecting solid angle from 4°-15° to 2°-10°. This choice of collecting angles admitted more background stray light which required careful filtering and aperturing to eliminate.

3. Calibration, Data Editing, and Combining Data Sets

The calibration of the two-dimensional Grey is via direct image registration methods. Each shadowed element is seen as an incremental area of approximately 1600 μm^2. Three shades of grey were provided for imaging (25%, 50%, and 75% contrast). Size bins are grouped every 40 μm by the DAS. Full image storage by the DAS is on an as-available basis. For acceptance, each image was required to have one pixel which reached 50% dark-level. This shadow density requirement in combination with the ER-2's true airspeed of 200 m s^{-1} effectively limits useful two-dimensional measurements to sizes larger than 80 μm. Still larger particles are required to determine crystalline habit.

The FSSP pulse height analyzer curves are set for the instrument's expected response to ice spheres based upon theoretical calculations and empirical tests. An empirical calibration of the FSSP was first performed with glass beads of refractive index equal to 1.51. Theoretical Mie calculations for glass beads and ice spheres were then compared to give the expected response to ice. The resulting calibrated size range for ice was 3-78 μm. The ASAS-X calibration of *Knollenberg et al.* [1982] was used for small aerosol.

The PSSE data set is only one of the sets of measurements required to characterize cloud environment. Of obvious additional need are the logistics and state parameter data. Certain other experiments provide further opportunities for comparison of microphysical quantities. All experiments aboard the ER-2 must have independent data acquisition and recording (essentially they must stand alone). Universal time is furnished all experiments for data synchronization; however, integration periods vary and, in the case of the PSSE, the 10-s integration periods can result in up to 10 s of uncertainty in exact data synchronization. Slight timing differences are evident in the data set comparisons between experiments. To a great extent these can be removed with manual editing.

The PSSE experiment has little size range overlap between the three individual instruments with one notable exception: the ASAS-X aerosol instrument has an oversize bin which can be used as a check against total particles measured by the FSSP and two-dimensional. Even allowing for some crystal breakup in transiting the ASAS-X plumbing, this cross-check proved invaluable when the FSSP's first channel was noisy. In the Australian data set it was found best to replace the more noisy FSSP first channel data with a residual bin representing the difference between the ASAS-X oversize bin and the FSSP's totals of channels 2-15. The noise level of the FSSP increases slightly with decreasing temperature and the -80° to -90° temperatures in Australia were significantly below any temperatures previously encountered with the PSSE. These extremely cold temperatures also resulted in frequent tape recorder malfunctions (rewritten data tracks) after cold soaking. Though little in-cloud data were lost, the latter sections of several flights were unusable.

The oversize bin of the ASAS-X was also useful for checking on possible ice crystal breakup. By integrating all sizes larger than 2 μm (including the oversize bin) and comparing FSSP and two-dimensional totals, the relative importance of crystal fragmentation could be weighed in contributing to the ASAS-X number density totals. This was examined by selecting a few regions of dispersed large crystals (two-dimensional active while FSSP inactive) and looking for increased activity in the ASAS-X. While we found that the influence on total ASAS-X number density due to crystal fragmentation was negligible, the ice water content increased significantly due to enhanced numbers of 1-to 3-μm sized particles. We attributed these to fragments of crystals larger than 100 μm since there was a paucity of FSSP activity in these cases. When crystals were smaller than 100 μm with little two-dimensional activity, no evidence for crystal breakup was suggested. That is, within FSSP noise limits the count correspondence between ASAS-X and FSSP over the size range overlap was reasonable.

The FSSP does not have the capability of generating an oversized bin with a defined sample volume; the sample volume definition scheme rejects all particles >78 μm. Thus there is negligible useful overlap between it and the two-dimensional for comparative purposes. The most accurate size range of this FSSP from crystal morphology and signal-to-noise considerations is from 10 to 60 μm. While noise influences the smaller size resolution and count accuracy, larger crystals mis-size due to orientation effects and scintillations from crystalline planes.

Because of the sizing uncertainties and unknown related ice mass, the total ice water content derived from the NOAA Lyman

alpha instrument [*Kelly*, this issue] was adopted. The NOAA ice water content was derived from their total water and water vapor instruments by subtracting water values and converting from parts per million to grams per cubic meter using pressure/temperature data. Comparing integrated ice water content from the PSSE allowed placing constraints on ice crystal bulk mass properties. When two-dimensional activity was high, area-to-mass conversions were possible to develop. When light scattering instrument data dominated, we elected to compute bulk densities from such comparisons assuming all the particles to be spheres. Tests for ice or water saturation were made by comparing computed saturation vapor densities with NOAA total water values. The main sources of error for the NOAA water instrument are the Poisson counting statistics of the photomultiplier, the uncertainty in the H_2O absorption cross section, and the calibration errors. The H_2O absorption cross section and the calibration error dominates for values over 5 ppmv and 10-s integration times. The total error approaches 6.6% with two sigma confidence for these conditions.

The University of Denver condensation nuclei (UDEN-CN) measurements (C. Wilson, unpublished material, 1992.) are a useful comparative measurement against total PSSE number densities. Using a similar inlet system, some crystal fragmentation also is likely, however, the influence on total number density of CN is generally negligible due to the much higher values of CN compared to ASAS-X particles.

4. Results

The STEP Tropical Experiment conducted during January and February of 1987 and based in Darwin, Australia, placed primary emphasis on mechanisms that could dehydrate the air entering the stratosphere. Previous measurements in Panama in September 1980 (Water Vapor Exchange Experiment (WVEE)) revealed that cumulonimbus activity in that region was more consistent with hydrating rather than dehydrating the stratosphere [*Kley*, 1982]. Dehydration requires that the bulk of the water be converted to ice crystals at the coldest temperatures found at anvil top. It is further required that these ice crystals be sufficiently large that they fall to lower levels prior to significant evaporation. It was, thus, necessary to postulate another source for the drier air found in the stratosphere over Panama. Micronesia appeared to be the primary candidate for yet colder regions with sufficient activity to desiccate a significant percentage of the stratosphere. Prior to the STEP Tropical Experiment, however, flights were conducted in continental cumulonimbus anvils in central Arizona during August 1986. These data offer a contrasting data set for comparative purposes.

4.1. *Continental Cumulonimbus Cloud Observations*

The summer 1986 cloud mission series of planned continental cumulonimbus penetrations was conducted on August 12 and 13, 1986. Because of the synoptic situation that existed during this time window, the region of interest was central Arizona. Moisture from the Pacific off the west coast of Mexico flowed northeastward over Baja across Sonora into south central Arizona generating vigorous cumulonimbus activity over Arizona.

The first flight with cumulonimbus anvil penetrations was on August 12. Approximately 2 hours into the flight, cirrus anvil outflow was penetrated at approximately 40,000 ft altitude (12-13 km) with temperatures ranging from -55° to -60°C. Multiple

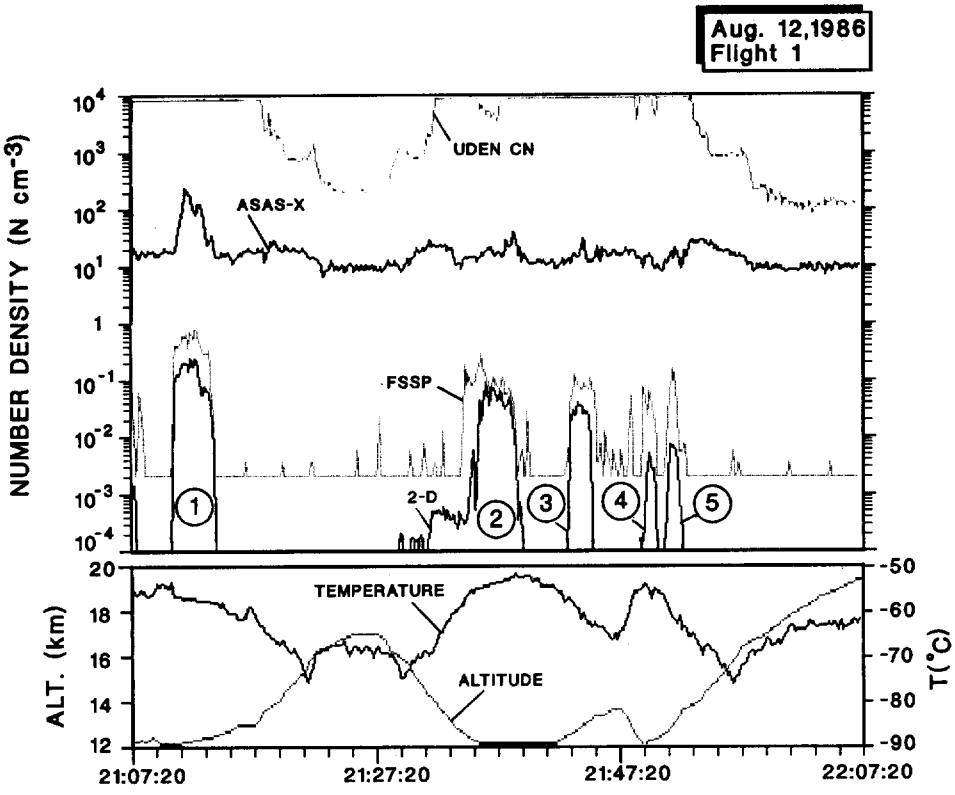

Fig. 1. Flight data for continental cumulonimbus anvil on August 12, 1986. The condensation nuclei (CN) counter has an upper concentration limit of 10^4 cm^{-3} and is saturated during most of the cloud passes. The FSSP number densities have been truncated to a lower limit of 2×10^{-3}.

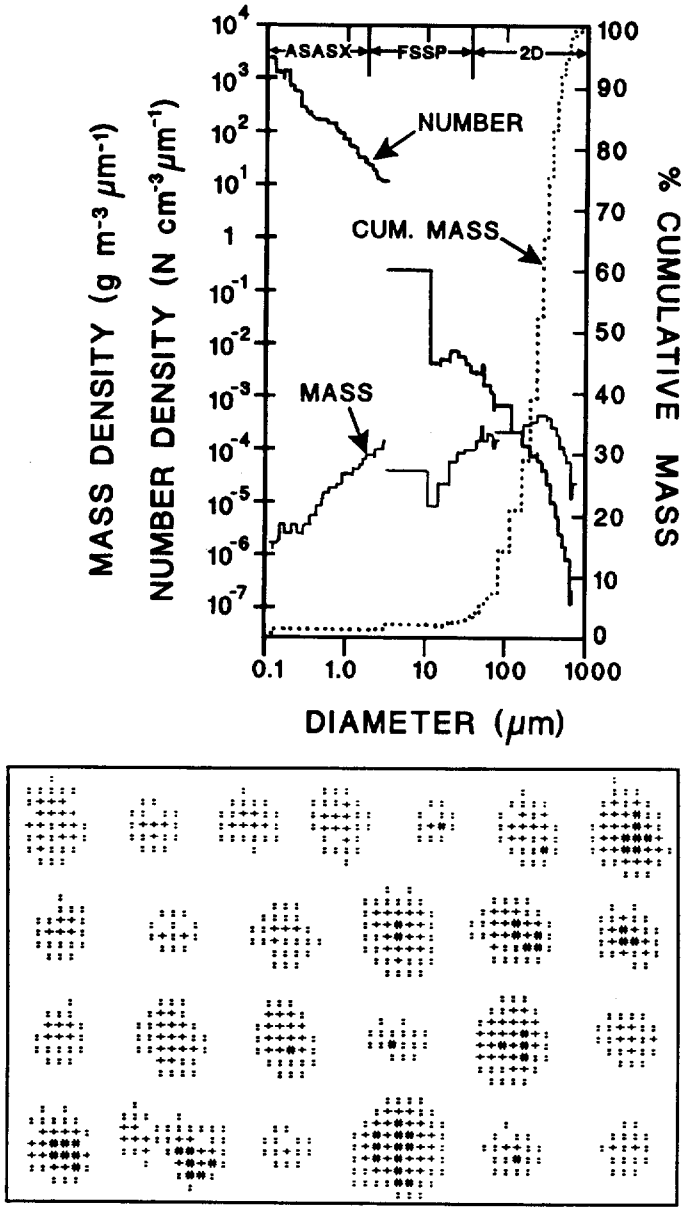

Fig. 2. Microphysical data sample for pass 1 of August 12, 1986, flight. (Top) size, mass, and cumulative mass distributions. The cumulative mass distribution indicates a mean mass crystal diameter of about 300 μm. There is a strong indication of fractionation contributing increased numbers of particles at the larger ASAS-X sizes. (Bottom) Image samples for passes 1, 2, 3, and 4 (in sequence, top to bottom).

passes (nine well-defined) over about a 1-hour period were clearly evident. Five of these passes were selected for detailed data analysis. These penetrations shown in Figure 1 revealed particle number densities up to 100 L^{-1} in the size range of the two-dimensional probe (this instrument contributed the bulk of the ice water measurement). Figure 2 presents size distributions and two-dimensional images observed during the densest cloud penetration during pass 1. The size distributions were observed to include particles from 0.1 μm to nearly 1 mm in size with reasonable agreement between the various instrument sections, although evidence of fragmentation is suggested at larger ASAS-X sizes. The images strongly suggest the majority of the crystals to be plates. Rarely were there any suggestions of aspect ratios greater than 1.5:1 discounting possible polycrystalline bullet-rosettes and bullets generally associated with cirrus [*Heymsfield and Knollenberg*, 1972]. In the range of size covered by the FSSP (3-78 μm), number densities increased to above 1 cm^{-3}, although the integrated mass was much less than that revealed in the larger ice crystal range of the two-dimensional probe. With regard to submicron aerosol the CN concentration was saturated (>10^4 cm^{-3}) most of the time in cloud, while the ASAS-X number densities reached maximum values of 100 cm^{-3} on pass 1; both instruments provided negligible mass contribution. The observed concentrations of CN in cloud-free air are considered typical of continental tropospheric air at these altitudes. Only during the most dense cloud pass (pass 1) do the ASAS-X number densities correlate with the increased activity observed on the FSSP and two-dimensional instruments.

On August 13 a second flight was conducted back to the central Arizona region. The cloud penetration was at a similar altitude and temperature as the August 12 flight and occurred

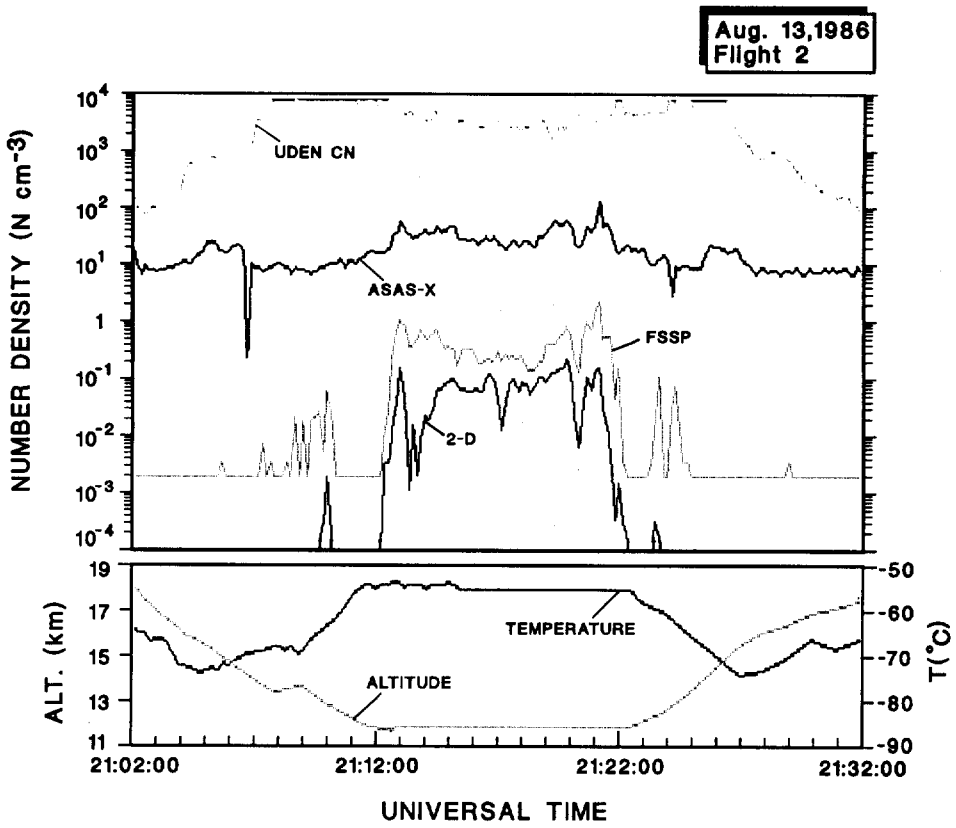

Fig. 3. Flight data for continental cumulonimbus anvil on August 13, 1986. The CN concentration was high but not saturated during this anvil penetration. The FSSP data have been truncated to a lower limit of 2 x 10^{-3}.

approximately 2.5 hours into the flight. Approximately 15 min of in-cloud data were obtained. During this cirrus anvil penetration the observed number densities shown in Figure 3 were less than those observed on the August 12 flight; however, the entire cloud mass appeared to be more uniform. Ice crystal concentrations (two-dimensional) were observed to be in the vicinity of 20-50 L^{-1}. Little increase in submicron aerosol activity was observed inside the regions of observed ice crystal activity. The CN averaged 3000 - 5000 cm^{-3}, while the ASAS-X averaged ~30 cm^{-3}. The CN reveals a negative correlation in cloud, while the ASAS-X only indicates a slight increase in activity in cloud. The size and mass distributions shown in Figure 4 are well behaved with good agreement among the ASAS-X, FSSP, and two-dimensional in the regions bridging the size ranges of coverage. Images were again predominantly of plates with some indication of more complex forms near the end of the cloud pass.

These data sets from these two flights provided the first opportunity for comparison with the NOAA-derived ice water contents. Data for the August 12 flight are shown in Figure 5 for the same five passes shown in Figure 1. The residual ice water content is revealed as the shaded areas defining the five cloud passes. It should be pointed out that there are two limitations to this kind of measurement. The first, which really applies only to the Australian data, is the finite noise level which typically amounts to about 5 X 10^{-5} g m^{-3}. The second limitation has to do with the ratio of ice water to water vapor. When the ice water is the overwhelming contribution to the total water (as in pass 1), the residual ice water measurement is more easily extracted than in cases where the total water and water vapor are nearly equal (as shown in passes 4 and 5). At this point it should be remarked that in most clouds the ice or liquid water content is less than the water vapor density. For instance, near the cloud base of a developing summertime cumulus with a temperature of 10°C a liquid water content of 0.5 g m^{-3} would be considered typical. The water vapor density at +10°C is, however, a much larger 9.4 g m^{-3}. In a mature cumulonimbus at -10°C, a liquid water content of 1-2 g m^{-3} would approach the water vapor density of 2.36 g m^{-3}. However, only in the tops (anvils) of cumulonimbus at temperatures below -40°C does one typically find ice water contents far in excess of the vapor density. It must be realized that the majority of this disproportionate ice water mass was condensed at lower altitudes and warmer temperatures and then convected to the higher altitudes and colder temperatures by strong convective activity. For our current purposes, situations like pass 1, where the ice water content is 5 times the vapor density, are more suitable for comparative study.

For purposes of comparison the task is to develop appropriate area-to-mass conversions for the image data and bulk densities for the FSSP size spectra that provide best agreement to the NOAA-derived ice water contents. Images processed assuming spherical shape (e.g., graupel) would result in an overestimate of particle ice water content of approximately 5 to 10 times. Since the imagery suggests plate crystals with the *a* axis in the plane of the images, we elected to test a correlation assuming hexagonal plate crystalline habit. Ice crystals are pristine and unrimed if formed at these temperatures. For sizes less than about 50 μm the *c* axis may be comparable to the *a* axis dimension and the crystal is nearly equidimensional. At larger sizes the *c* axis remains approximately 50 μm in dimension. It is

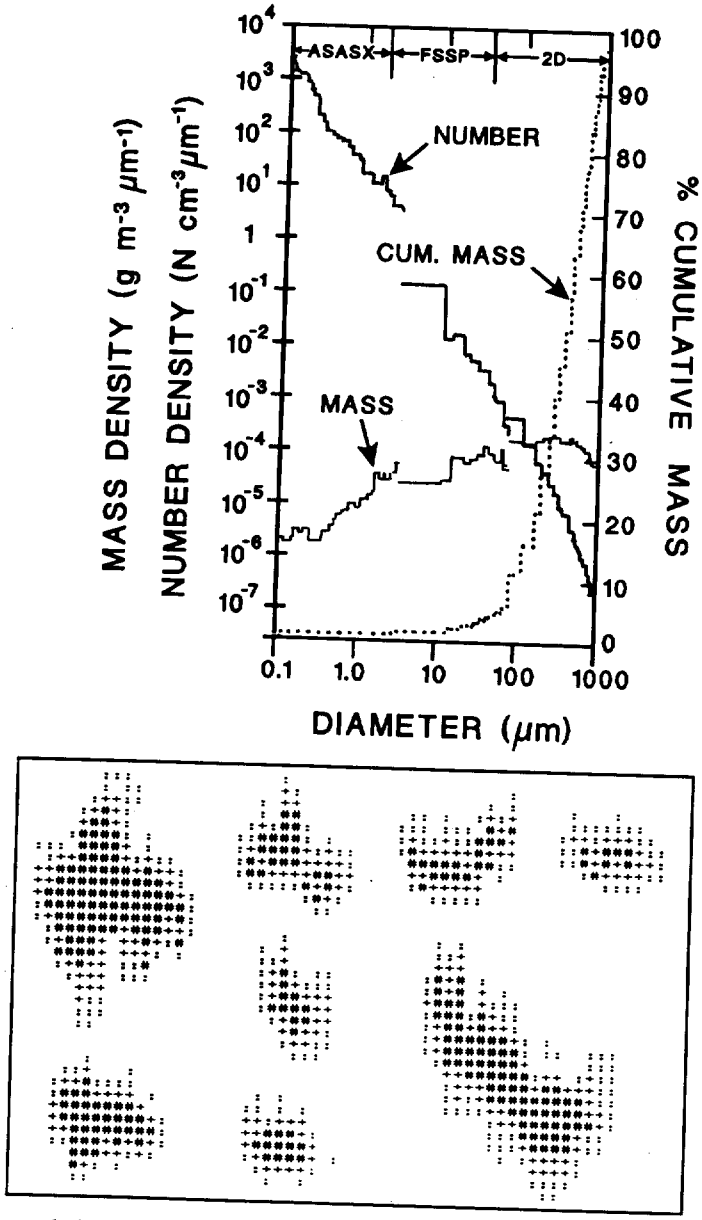

Fig. 4. Microphysical data sample for pass 1 of August 13, 1986. The size and mass distributions for this flight revealed less indication of fractionation contributions at the larger ASAS-X sizes. This image sample is from the last 3 min of the cloud penetration. The remainder of the cloud penetration produced images very similar to that in Figure 2.

characteristic of such plates to have truncated growth in the *c* axis. The mass of a crystal in grams may thus be represented by $m = 0.005A$ where A is the crystal plate area in square centimeters. This turned out to be the best correlation found for the image data for both August 12 and 13. Because of the high similarity in axial dimensions and high bulk density for plates or other crystal types at sizes smaller than 50 μm, the FSSP data was processed using a light scattering response of equivalent spherical sizes and a bulk density of 0.9 g cm^{-3}.

The mass correlations for the flights on August 12 and 13 are shown in Figures 6 and 7. For the first three passes on August 12, excellent correlation is found between the NOAA ice water content and the derived water content from the two-dimensional image data alone. Here the FSSP was found to contribute only 10-20% of the ice water mass. For passes 4 and 5 the contributions from the FSSP and two-dimensional image data are nearly equal and, when added together, they provide a reasonable fit to the NOAA ice water content. On August 13 with the imagery again suggesting hexagonal plates to be the dominant crystalline form, we were again able to obtain reasonable agreement in the ice water contents, as shown in Figure 7.

These data can be further examined by means of the scattergrams shown in Figures 7 and 8. The correlation coefficients of $r = 0.82$ and $r = 0.95$ as well as the obvious signature similarity revealed by inspection of Figures 6 and 7 suggest that a significant amount of the variance is explained. Improved correlation can be obtained on August 13 by injecting a habit change in the last third of the cloud pass. The image data in Figure 4 suggest a more complex or a polycrystalline structure for the larger crystals with darker shadow densities implying greater thickness. If one doubles the crystal thickness of these large crystals which doubles the mass the correlation improves to $r = 0.96$.

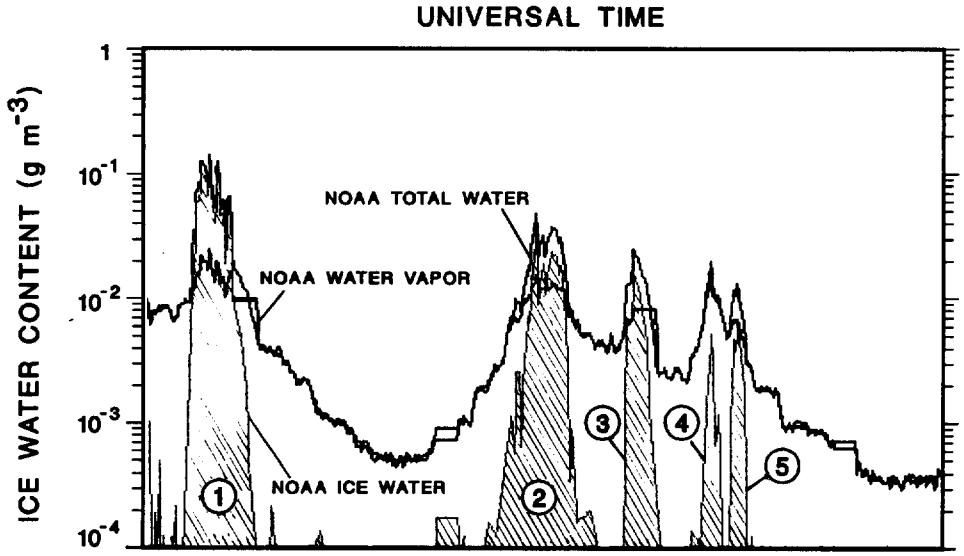

Fig. 5. Flight profiles of NOAA water measurements. The ice water content was derived from subtracting water vapor from total water and is shaded.

These August experiments turned out to be of considerable importance in providing some of the few opportunities to develop area-to-mass correlations. During the following Australian experiments, ice crystal sizes at cloud top were rarely large enough to exhibit measurable contributions from the two-dimensional imagery. At the much colder temperatures near the tropical tropopause, maximum crystal dimensions were consistently less than 100 μm. Thus the two-dimensional imagery provided no measurable useful habit information.

4.2. *Tropical Cumulonimbus Cloud Observations*

The STEP Tropical Experiment Darwin flight series was planned to coincide with the summer monsoon season where the coldest cloud top temperatures have been observed. During this period of time our primary interest focused on the coldest available systems including less organized systems as well as tropical cyclones. The PSSE data analysis concentrated on two active monsoon periods where cloud penetrations were a primary goal in experimental design. The first flight selected for detailed analysis was flight 9 on January 31, 1987. Cyclone Damien was developing west of the Kimberlies in Northwest Australia providing active bands of strong convective activity to the north of Darwin. North-northeast to south-southwest flight paths at several levels with horizontal legs perpendicular to the cloud band structure were conducted to measure cloud heights, water vapor, and ice crystal mass distributions.

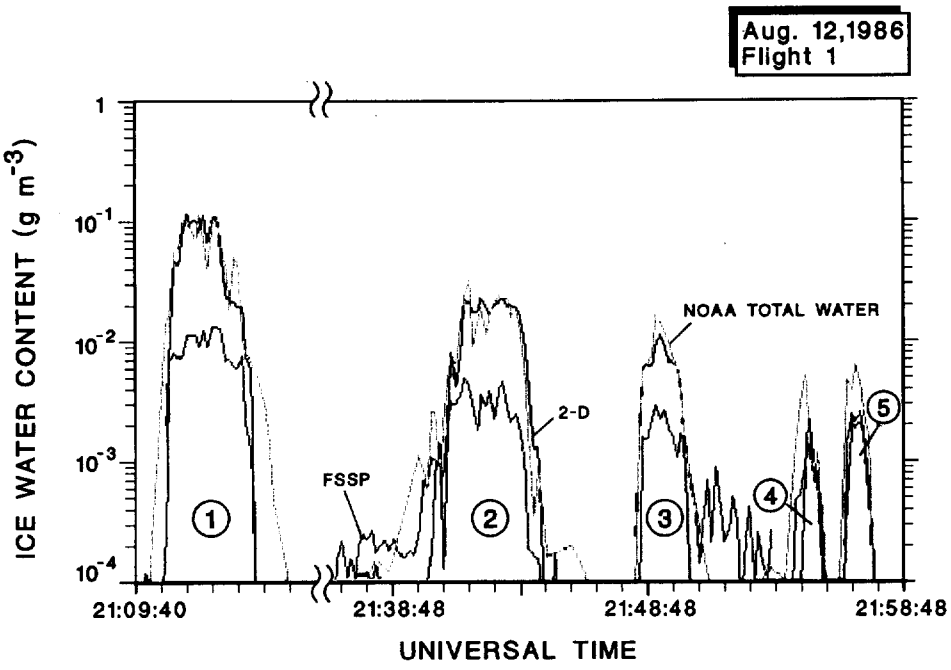

Fig. 6. Comparison of NOAA total water and integrated water from two-dimensional and FSSP instruments for August 12, 1986. For the first three passes, the two-dimensional contributes greater than 90% of the total water, while for passes 4 and 5 the FSSP and two-dimensional contributions are comparable.

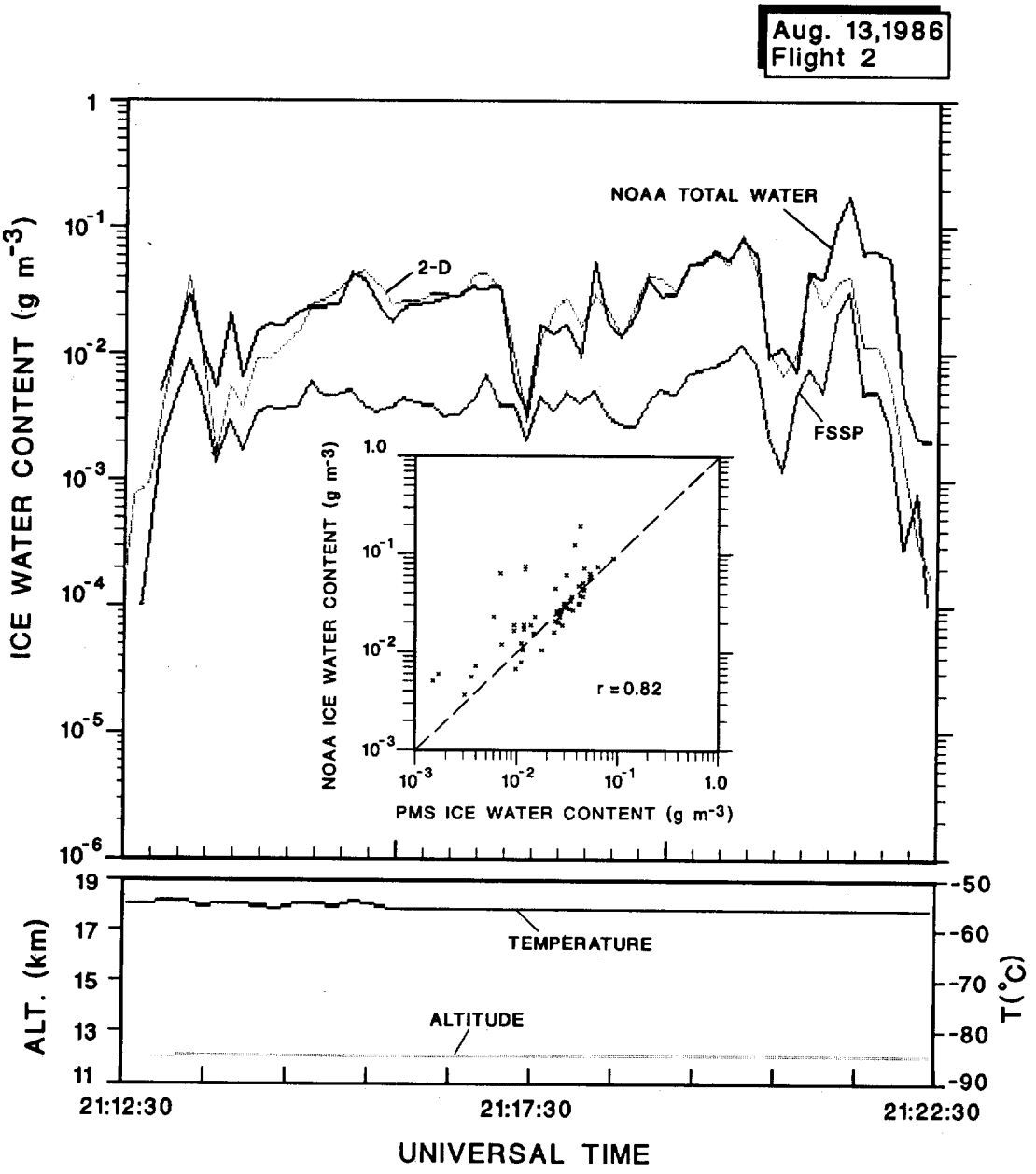

Fig. 7. Comparison of NOAA total water and integrated water from PSSE instruments for August 13, 1986.

This flight provided the first opportunity to investigate extensive convection along long horizontal legs. Descending to 15.3 km from a cloud-free leg at 18.3 km, cloud penetrations at increasing altitudes were initiated. The strongest cell was penetrated at about 15.5 km. Figure 9 shows the activity for the PSSE instruments as well as UDEN's CN data. In the stratospheric air at 18.3 km, number densities of CN (20 cm^{-3}) and ASAS-X aerosol (5-10 cm^{-3}) differ only by about a factor of 3 which is typical of tropical stratospheric cloud-free air. After descent to 15.3 km and just prior to entering the cloud region, the ratio of CN to ASAS-X increases to 2 to 3 orders of magnitude (typical of tropospheric cloud-free air) with the CN primarily anticorrelated with cloud activity. Only during the strongest activity encountered at 15.5 km do we see a slight corresponding increase in CN. This particular cloud system appeared to be strongly influenced by tropospheric air as evidenced by the high CN, strong convection and turbulence, and high ice water content values (0.05-0.07 g m^{-3}). The coldest temperatures encountered were -83°C, which are warmer than the other cloud systems investigated. *Danielsen* [this issue] suggests this is typical of maritime storms; those with more continental influence result in colder cloud tops.

The region of strongest convective activity at 15.5 km is expanded in Figure 10 where we compare the NOAA total water, NOAA ice water, and PSSE ice water derived from the FSSP and ASAS-X instruments (hereafter PMS ice water). Statistical correlation results are shown in Figure 11. The strongest cell took approximately 10 min to transit corresponding to a path length of 120 km. The PMS ice water arises almost entirely from the FSSP measurement. Ice water contents reaching 0.07 g m^{-3}, at temperatures of -78°C, correspond to nearly 100 times that found in the vapor at ice saturation. As the data reveal, when the ice water contents approach values similar to that of the vapor, correlation is less pronounced, as would be expected since the

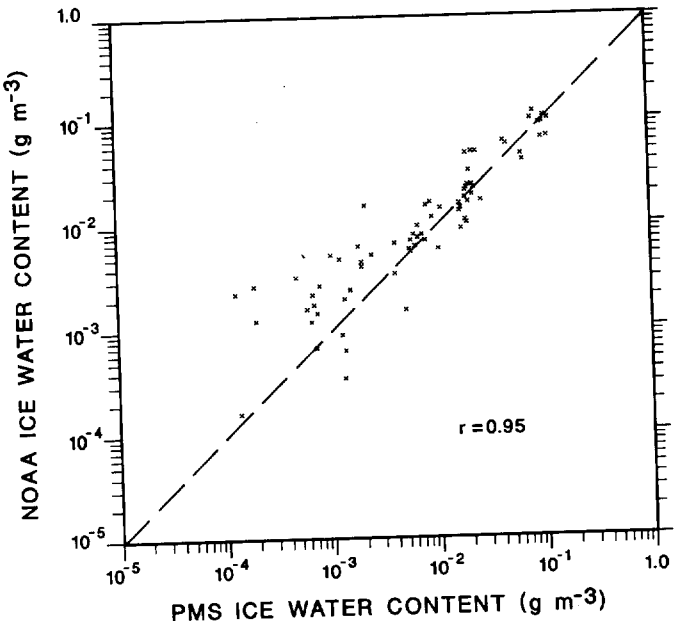

Fig. 8. Scattergram comparing NOAA ice water and PMS PSSE ice water for August 12, 1986, flight.

ice water content measurements are within the uncertainty of the total water content measurements. The size, mass, and cumulative mass distributions for selected regions (numbered in Figures 9 and 10) are displayed in Figure 12. The ambient stratospheric aerosol in region 1 is typical of that encountered during most stratospheric sampling of H_2SO_4 aerosol. The number distribution is exponential with a fairly abrupt cutoff at about six tenths of a micron. In the strongest cloud region (region 3) there is revealed the development of a strong mass mode around 30-40 μm, while the weakest cloud region (region 4) reveals a mass mode of only 5-6 μm. The largest two-dimensional particles observed were less than 100 μm in size and without recognizable image form.

The second flight selected for study was flight 11 on February 3, 1987. It was one of great interest in terms of microphysical cloud characteristics. Cyclone Damien had developed into cyclone intensity and was the subject of this flight to the southwest of Darwin. In retrospect, Cyclone Damien was found to be in a state of decline at the time these measurements were made. After a traverse over the anvil top, the ER-2 turned southeast and descended to enter cloud on the western edge. It then turned and made a traverse to the northeast within the anvil (Figure 13). During descent the cloud top was found to be at 16.4 km at the base of a strong inversion. Approximately 40 min of in-cloud, data were obtained at altitudes ranging from 14.6 to 17 km (Figure 14). The lapse rate was nearly adiabatic. Exiting the cloud at 17 km, a stronger inversion was encountered with temperatures of -90°C, the coldest values measured by the ER-2 during STEP. The enhanced infrared image of Figure 13 reveals that near entry the cloud had an effective radiative emission (cloud top) temperature of -60°C. The in-cloud northeast traverse passed through regions with radiative emission temperatures of -80°C. This flight passed to the north of the eye wall and was surprisingly turbulence free. This entire cloud region is in reality quite large, some 500 km in extent with nearly 150 km with cloud top radiative emission temperatures of -80°C. Differences between radiative emission temperatures and ER-2 measurements reflect variations in cloud emissivity and thickness. In general, minimum anvil cloud top temperatures are at least 5°-10°C lower than the satellite radiative emission temperatures.

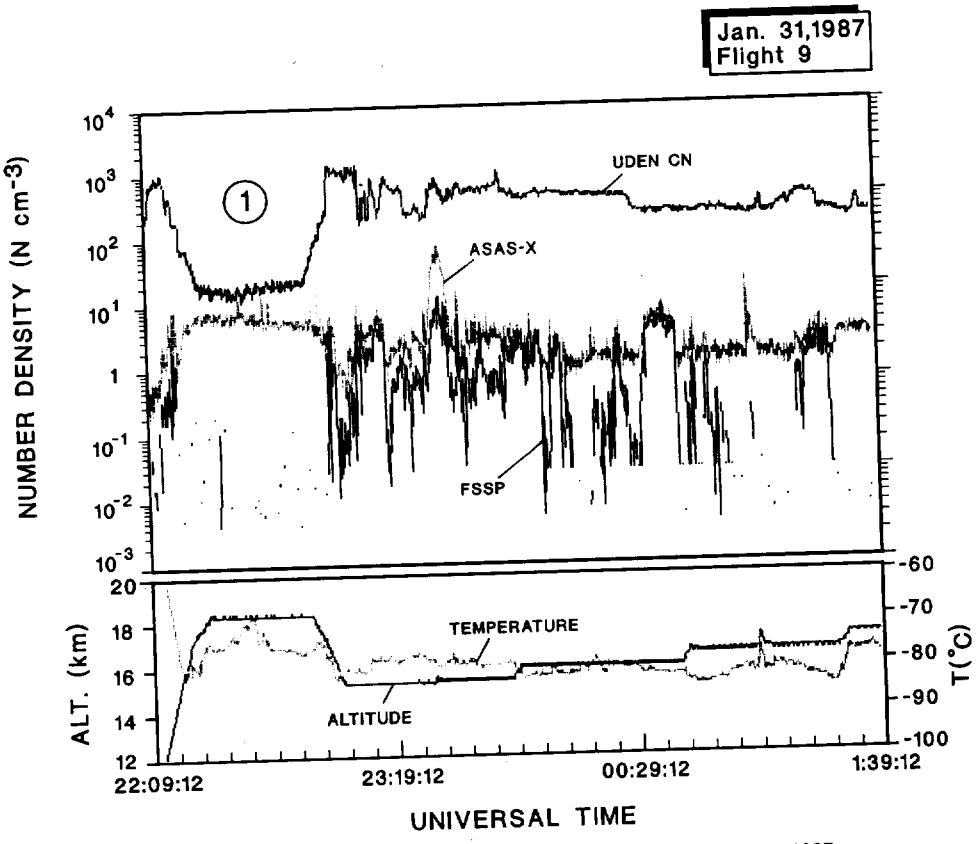

Fig. 9. Flight data for tropical cumulonimbus anvil flight on January 31, 1987.

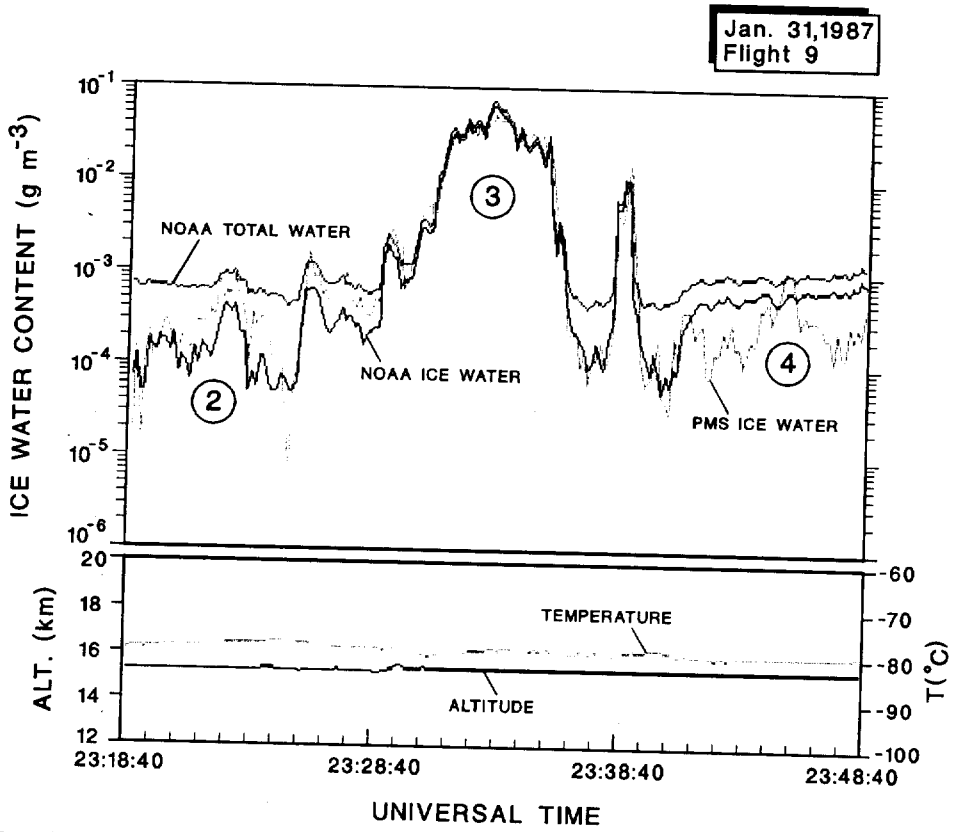

Fig. 10. Comparative water measurements for most active region observed on January 31, 1987, flight: Essentially all of the particle ice water content is derived from the FSSP. The derived NOAA ice water content in pass 4 was influenced by water contamination revealed in the lack of correlation here as compared to pass 2.

Figure 14 shows the particle concentrations observed for the cloud pass. At the higher altitudes of this cloud pass, the signature correlation among the ASAS-X, FSSP, and CN instruments is extremely close, suggesting that most of the CN are actively involved in the cloud's microstructure or cloud hydrometeors actively scavenged the smallest CN. The only area of noteworthy difference is around 0335:00 where a large peak in CN is observed to be anticorrelated with cloud particle number density. This appears to be a region of stronger continental tropospheric influence, as was evidenced by the high radon activity (20 pCi/scm) reported by *Kritz et al.* [this issue]. At the colder temperatures the total number of PSSE cloud particles is essentially the same as the CN, while at somewhat lower altitudes the CN averages about 3 times the total number of cloud particles measured. Because of the strong signature correlation between CN and cloud particle instruments we believe that essentially all CN particle measurements reflect active cloud particles (ice crystals). One does not have to extend the ASAS-X size spectrum (e.g., lognormal fit) much below 0.1 μm to accumulate totals equal to the CN at any level. This region stands in stark contrast to that of Figure 9 where even in the most active region the CN were at least an order of magnitude higher than the total number of cloud particles.

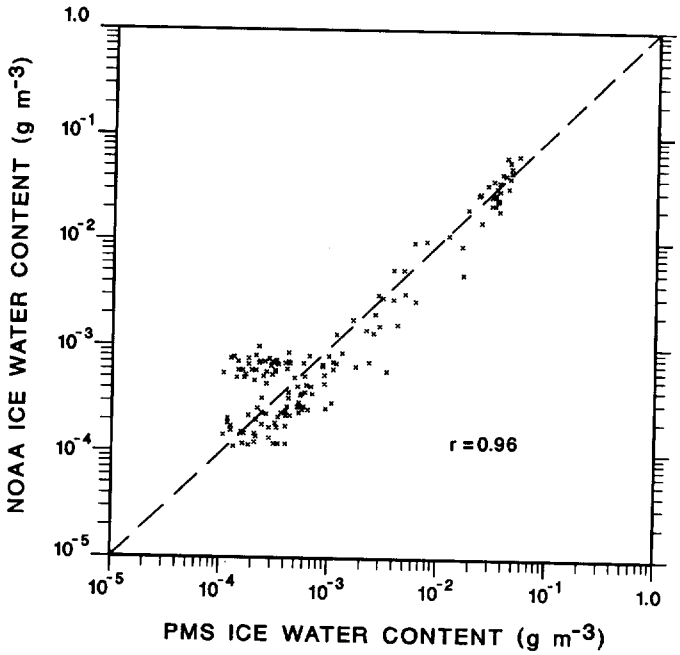

Fig. 11. Scattergram of comparative ice water measurements for January 31, 1987.

The coexistence of the smallest and largest of these particles is only consistent with a supersaturation with respect to ice and further suggests rampant ice nucleation has occurred. The ability of small CN to first behave as CCN (and subsequently as IFN) ordinarily requires relative humidities only several percent less than water saturation. This corresponds to 90-100% supersaturation with respect to ice at cloud top temperatures. Such high supersaturations are difficult to support and in fact were not observed. That the observed maximum sizes during this period, as revealed in Figure 15, are still less than 100 μm and median mass sizes are ≈ 30-50 μm are indicative of: (1) the relatively slow growth rate and (2) the

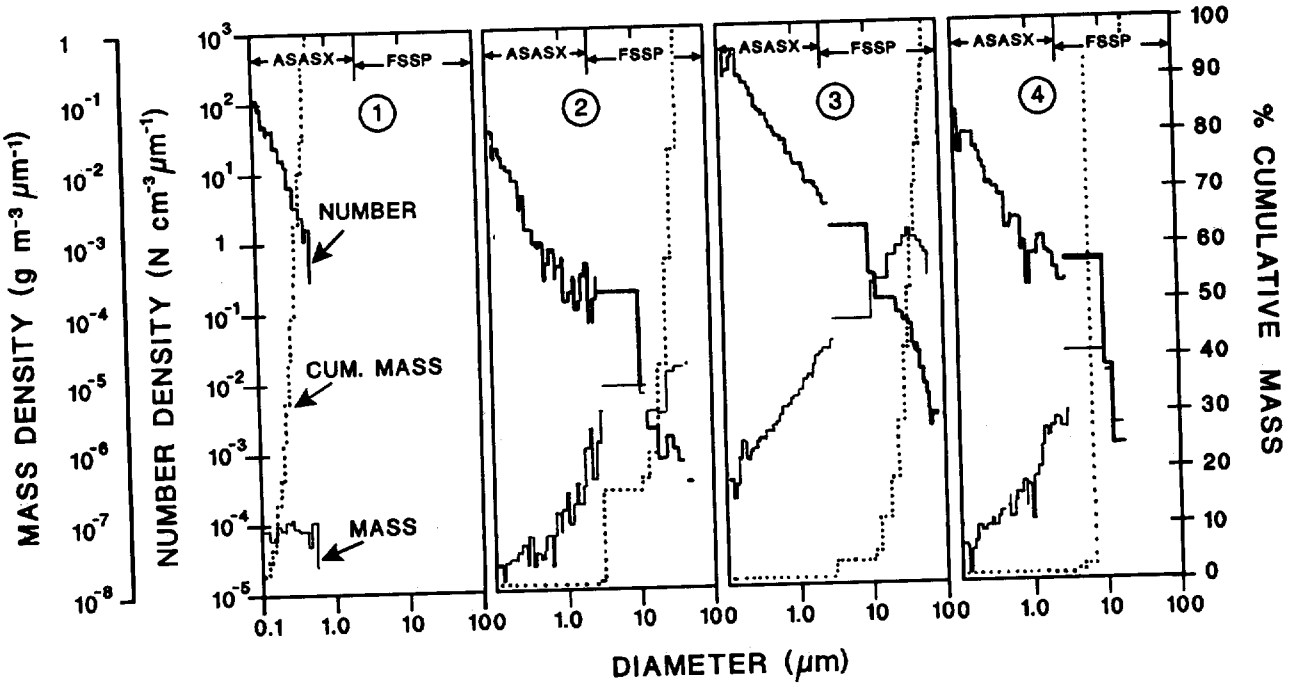

Fig. 12. Ice crystal distribution for January 31, 1987. These distributions for each of the four passes include samples of stratospheric aerosol (region 1) regions of relatively low water content (regions 2 and 4) and a region of fairly high water content (region 3).

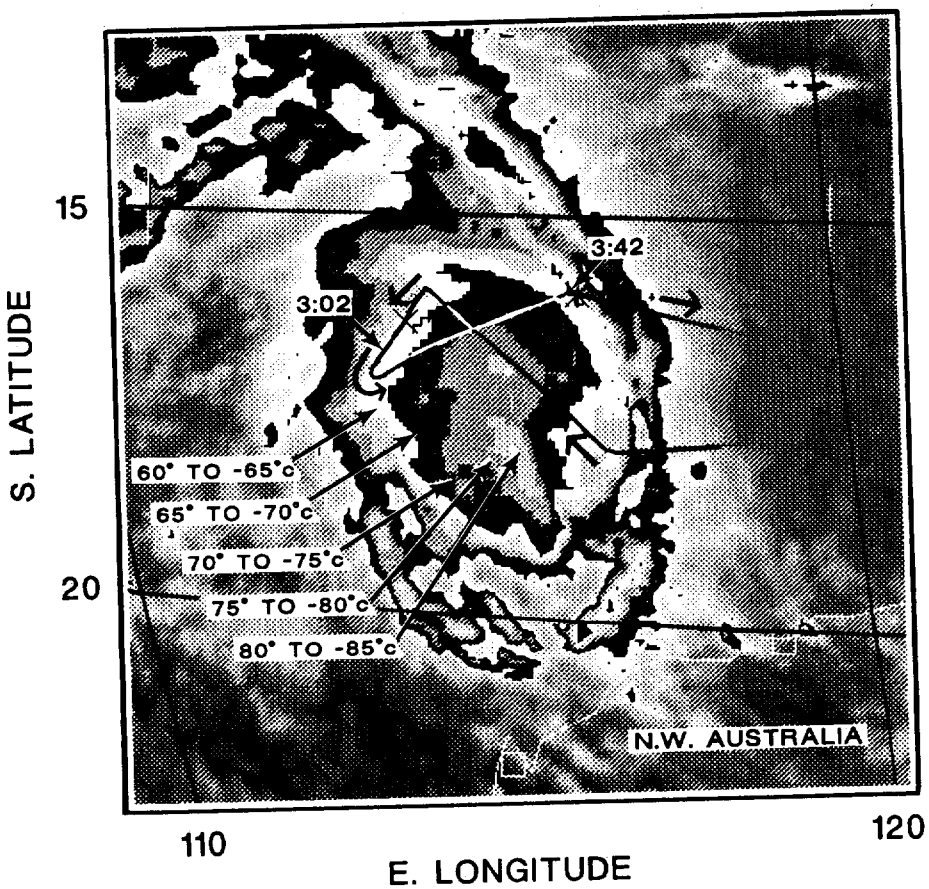

Fig. 13. GMS-enhanced infrared image on 0300 UT on February 4, 1987, covering tropical Cyclone Damien offshore of the northwestern coast of Australia. Flight path for flight 11 superimposed: Times shown are for entering and exiting the cloud top. The flight trajectory indicates sampling did not occur in the coldest region. According to radiative emission temperatures shown the coldest, or at least optically thickest, anvil region was approximately 160 kilometers south of the flight path.

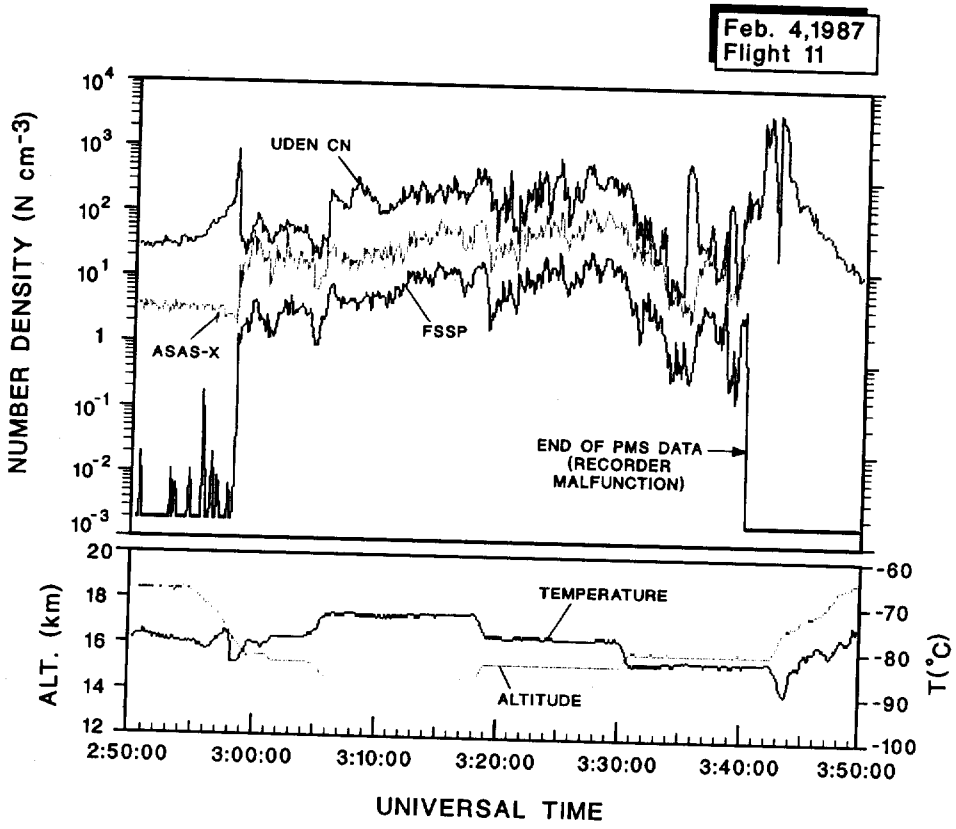

Fig. 14. Flight data for anvil flight 11 on February 4, 1987, in the top of tropical Cyclone Damien.

strong competition between the crystals for water vapor. Both suggest low supersaturations.

It is noteworthy that the strongest correlation between NOAA and PMS ice water contents here is not at values of maximum ice water content but rather at the lower values. The comparative ice water contents of Figure 16 do, in fact, show some regions (e.g., region 2) where the PMS ice water is less than the NOAA ice water. This is outside the range of experimental error for such mass comparisons despite the fact that the correlation coefficient of 0.92 remains high. It is our opinion that this

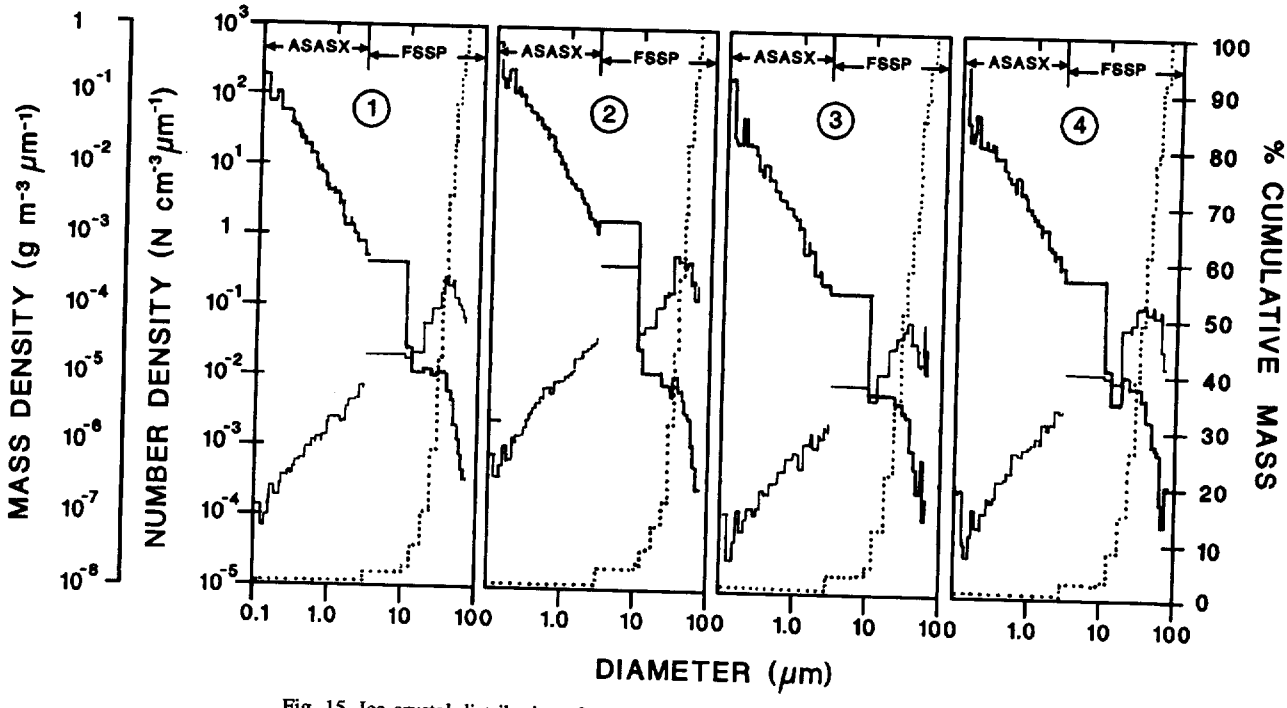

Fig. 15. Ice crystal distributions for regions of anvil pass indicated in Figure 16.

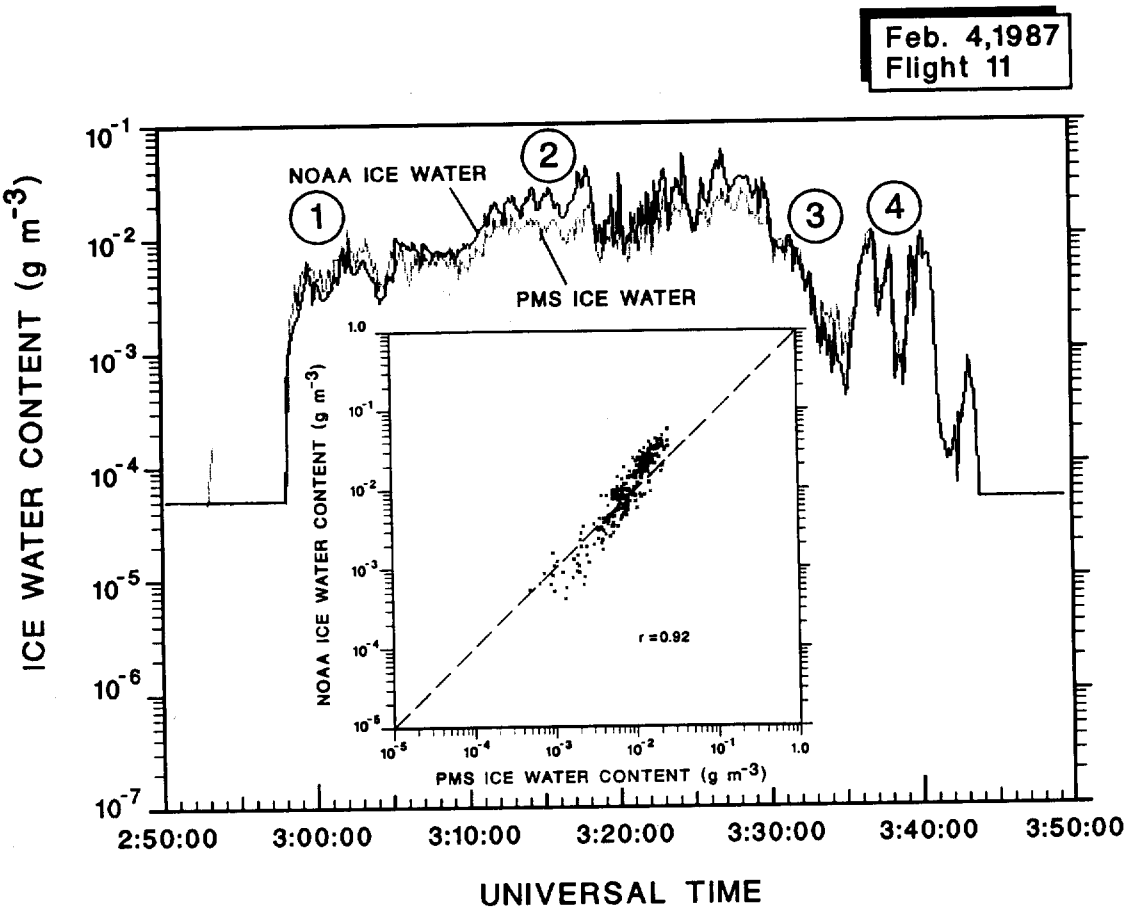

Fig. 16. Comparative ice water content measurements for flight 11 on February 4, 1987.

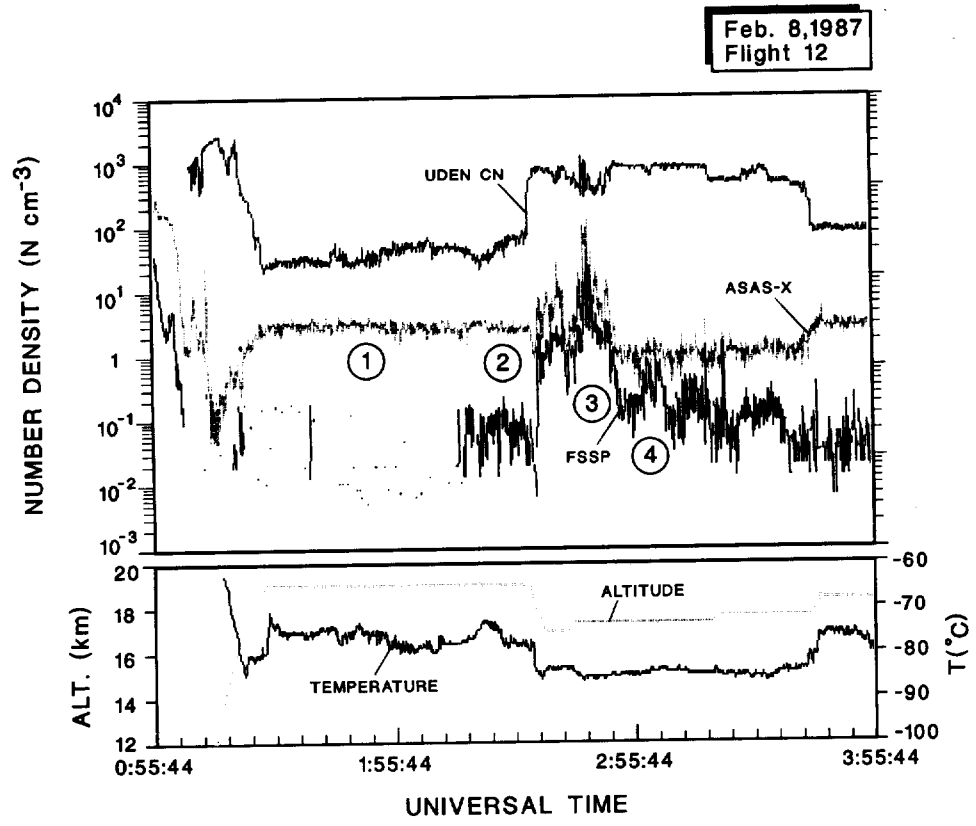

Fig. 17. Flight data for tropical cumulonimbus anvil flight 12 on February 8, 1987, in tropical Cyclone Jason.

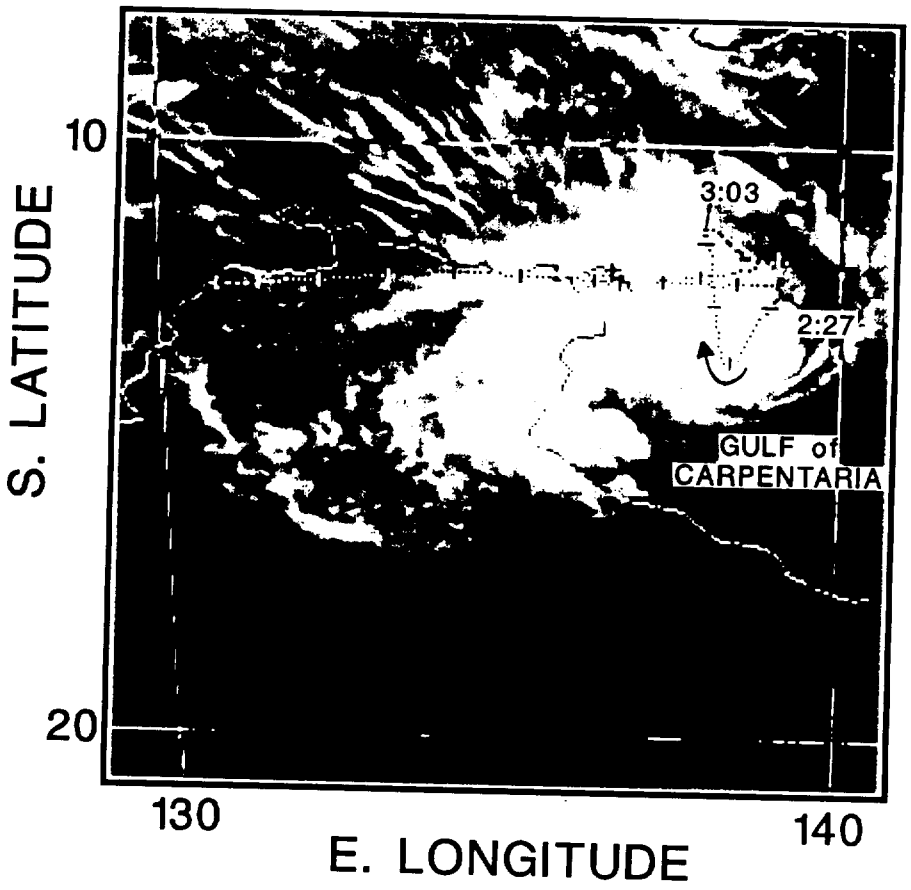

Fig. 18. GMS infrared image for 0300 UT on February 8, 1987, of tropical Cyclone Jason located at the northwestern end of the Gulf of Carpentaria. Flight path for flight 12 superimposed.

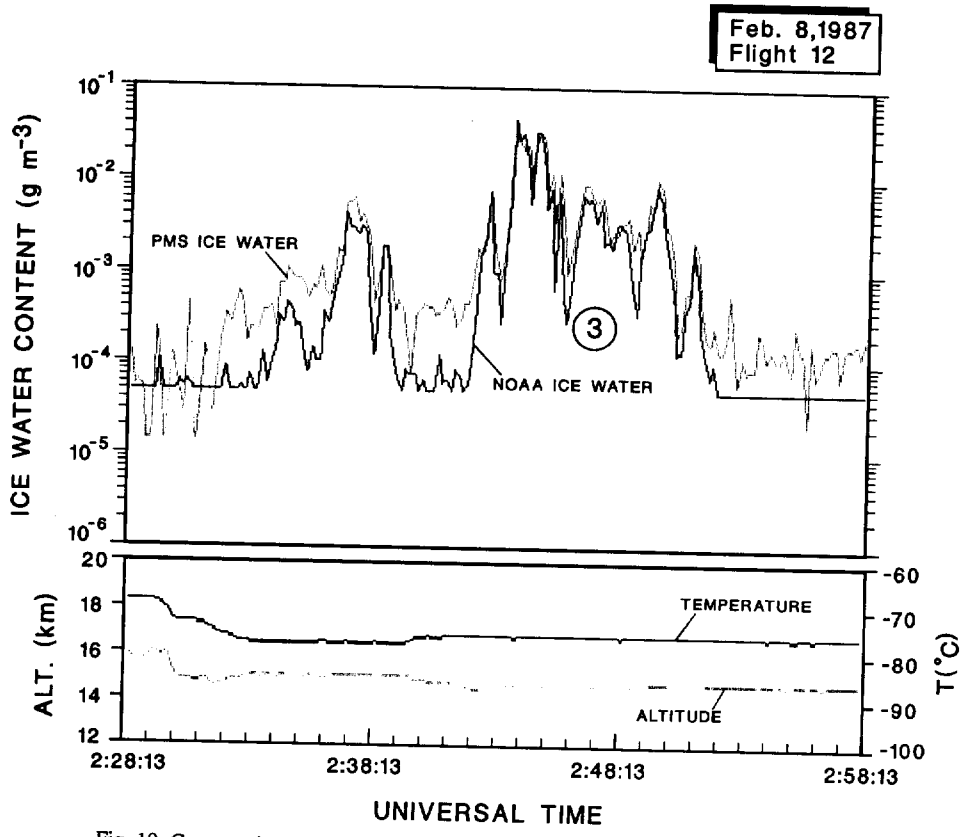

Fig. 19. Comparative ice water content measurements for flight 12 on February 8, 1987.

region represents a reduction of FSSP sample volume (likely due to fouled optics) since the first channel of the FSSP (derived from FSSP and ASAS-X oversize data) is artificially high.

The final flight of interest during the Darwin series provided penetrations into the tops of the anvil of Cyclone Jason. This fourth cyclone of the monsoon season developed over the northern gulf of Carpentaria. The flight, directed to the east of Darwin, first passed over the cirrus cloud shield followed by a descent and a traverse to the north just skimming the cirrus cloud tops (Figure 17). After completing this traverse and descending into the anvil, the ER-2 encountered severe turbulence and the pilot increased altitude abruptly and then conducted the remainder of this northerly traverse with subsequent steps to avoid turbulence. As shown in Figure 18, the ER-2 first encountered the cloud region just after 0230:00 after descending from 18.2 to 16.7 km. Satellite-enhanced images show that this flight clearly passed through the coldest cloud region with minimum in-cloud temperatures of -87°C at 16.7 km. Comparison of the CN with cloud particles reveals that only in the strongest cloud region do the total number of cloud particles approach within an order of magnitude the total number of CN with no perceptible correlation to cloud activity. The strongest region of cloud activity was penetrated between 0228:00 and 0258:00. In the most intense cloud region, ice water contents approached those of flight 11, but in most areas the ice water content was much less, as shown in Figure 19. The extraction of ice water content from the NOAA instruments has been truncated at 5×10^{-5} g m^{-3} because of noise considerations. A scattergram revealing a correlation coefficient of $r = 0.95$ for this region is shown in Figure 20. Regions beyond 0300:00 until 0355:00 reveal measurable cloud particle numbers but with vanishingly small ice water contents. In the weaker cloud regions of this flight there is strong evidence that the ice crystals are in regions of subsaturation and some have sublimated. The ice crystals observed in regions 2 and 4, as shown in Figure 21, reveal two independent populations of submicron aerosol, one

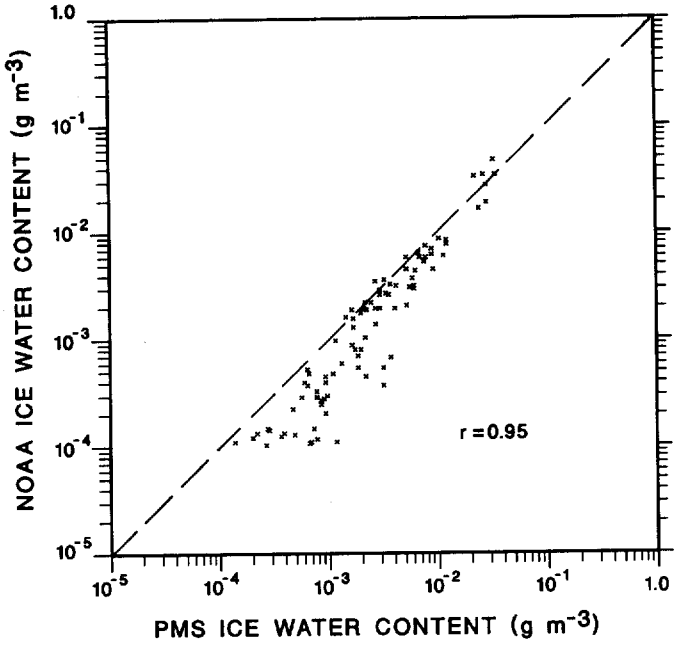

Fig. 20. Scattergram of comparative ice water measurements for flight 12 on February 8, 1987. The lack of a 1:1 correlation at low water contents is probably due to instrumental factors.

population resembling region 1 in stratospheric air and the other populations that of dispersed 10-to 20-μm ice crystals. These are to be contrasted with the continuous distributions revealed in region 3 of more vigorous cloud development.

5. Discussion and Analysis

The data just presented are unique in a number of respects, especially in the extremely high number densities and the large ratio of ice water to vapor observed. These are also undoubtedly

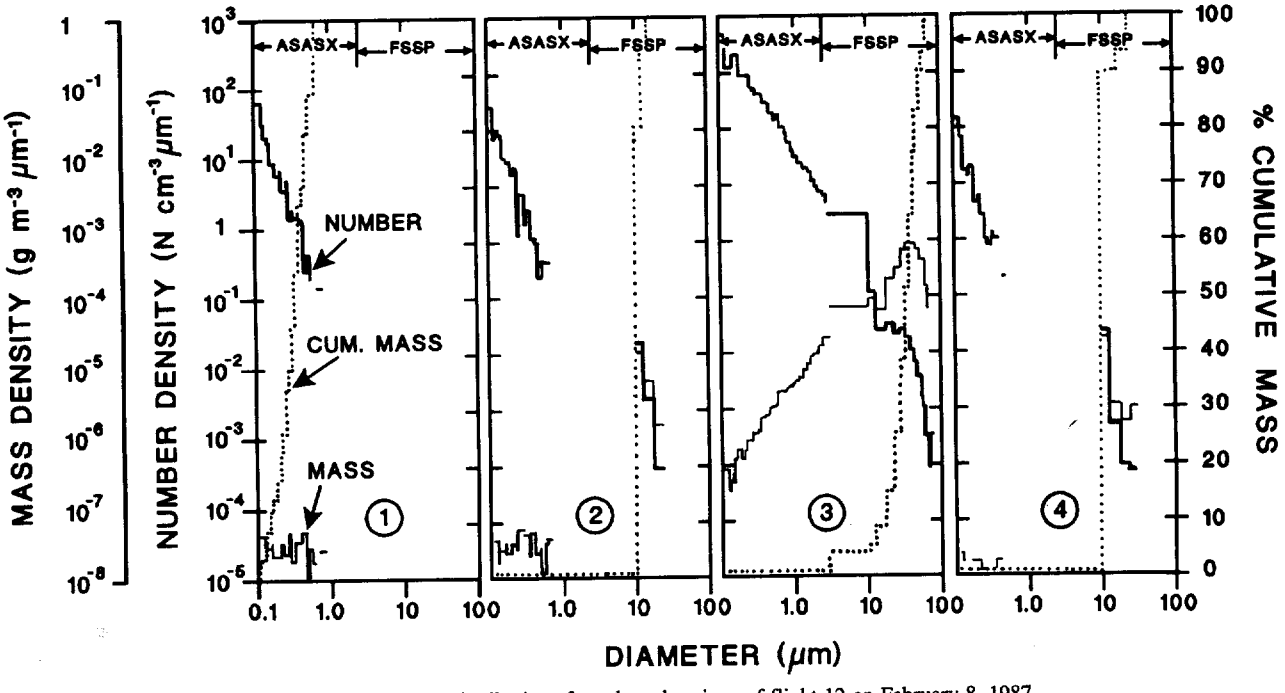

Fig. 21. Ice crystal distributions for selected regions of flight 12 on February 8, 1987.

the coldest temperatures at which measurements of this kind have been made and it is interesting to examine the microphysics in this unusual regime. Whether hydration or dehydration results largely hinges upon the ultimate fate of the ice crystals at the highest altitudes. The excellent correlation between computed ice water content (using particle number densities and size) and measured ice water content was rather surprising considering the extreme environmental conditions and deserves explanation.

With regard to the correlations between the computed ice water contents from particle size distributions and that of the NOAA measurements, there are several factors which contribute to the observed good agreement. Most important is that we have adopted the NOAA-derived ice water contents as correct and then simply determined either the bulk density or the area-to-mass relationship providing best agreement. In the case of the tropical Australian data it was simply necessary to assume that the particles were spheres, while the continental U.S. image data necessitated a selection of crystalline habit and a choice of crystal thickness to provide best agreement. When ice crystals are quite large, they are preferentially oriented making habit differentiation more certain when using two-dimensional data. Crystalline plates larger than 100 μm are thus ordinarily preferentially oriented and the largest projected areal cross section is measured. (The thickness was not measured, although the two-dimensional (Grey) provides measurements of opacity which correlate with thickness and structure.) That these crystals were found to be treatable using such a simple relationship on two different days over wide regions is probably more indicative of the homogeneity in this regime than the precision of the measurement. The rather good agreement between the FSSP and the NOAA ice water contents implies that the spherical assumption used (low aspect ratio) is appropriate. We were rather surprised by the lack of larger imageable crystals and apparent lack of variety in ice crystal forms. This must be contrasted with anvil measurements in Panama [*Knollenberg et al.*, 1982] which at only slightly warmer temperatures revealed ice water contents equivalent to those measured here but entirely derived from crystals larger than 40 μm in size with mean mass sizes of 400-500 μm and aspect ratios generally exceeding 2:1.

It is somewhat more surprising to find the additional good agreement between the "nonimaging" FSSP (assuming solid ice spheres) and NOAA values in Australia. At very cold temperatures, ice crystals develop polycrystalline habits and are often quasi-spherical (or at least have low aspect ratio) and are quite dense [*Heymsfield*, 1986]. A high density is not unusual for small ice crystals. Thus for small crystals a solid sphere assumption can be quite satisfactory for computing volume and mass. The correlative measurements are remarkably good considering prior experience with standard FSSP measurements in ice crystals. Here we have to be careful, however, because this particular FSSP had two important functional differences. First, the beam cross section is much larger at 4 X 0.5 mm while a standard FSSP has a circular beam cross section of only 0.2-mm diameter. Second, the width of the sample volume was defined by an imaging method, whereas in a standard FSSP the sample volume width is derived from transit time measurements. In the standard FSSP a variety of crystalline types can develop a weak scattering response through partial illumination (i.e., bulk of crystal lies outside the beam) and still be accepted as valid measurements. The net effect is overcounting while undersizing. Such a condition is not possible in the current configuration because, with the large beam dimensions and use of the imaging method to define sample volume width, the accepted measurements are always derived from fully illuminated crystals with optically defined sample volumes. While it may be surprising that the relationship appears valid over a wide range of cirrus anvil environments, it is not totally unexpected. Small solid crystals of low aspect ratio provide an average scattering response nearly equivalent to spheres of equivalent volume or mass.

Turning to the crystal sizes and numbers observed, it is important to have a good estimate of the mass and size of crystals not simply from the standpoint of estimating ice water content but to provide reasonable estimates of mass transfer (rates of growth or evaporation) and sedimentation. With regard to desiccation mechanisms it is most important to determine whether the mass is likely to be transferred to lower levels prior to potential measurable hydration (sublimation) at altitude. Probably the most interesting case to treat is flight 11 which, in addition to providing sizable uniform ice water contents, was also a case in which the total number density of measured cloud particles came closest to matching the total CN. At first glance the strong correlation among CN and ASAS-X and/or FSSP signatures implies that most CN here are involved in cloud processes. In order for this to be true, sufficiently high supersaturations must have developed at some point in the cloud life cycle to activate additional CN as CCN and subsequently as IFN. Thus one question to be explored is whether it is possible for new nucleation to occur in the presence of the observed ice crystal spectrum. Growth rates of the measured size distribution can be balanced against possible updrafts and observed temperature profiles to see if the necessary saturation ratios can be achieved.

While no attempt at numerical modeling was made, it was found useful to perform key microphysical computations to examine possible dehydration/hydration and nucleation processes in

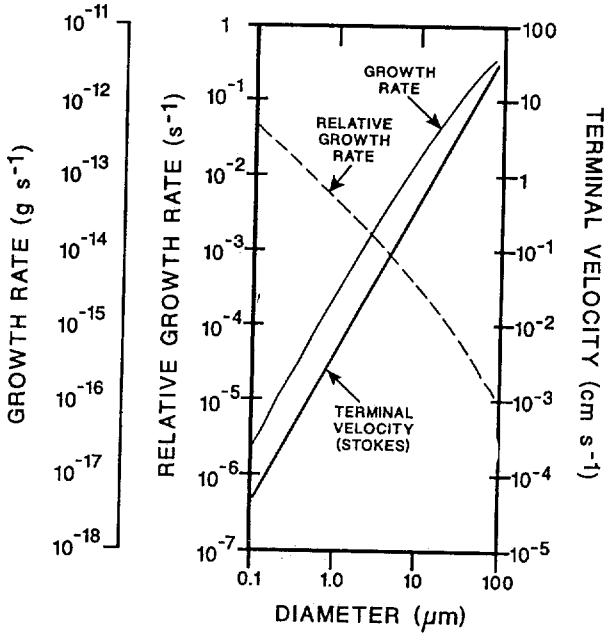

Fig. 22. Ice crystal growth rate and terminal velocities in tropical cumulonimbus anvil environment: These computations used the following derived parameters: Water vapor diffusivity (D) = 0.95 cm^2 s^{-1}; thermal accommodation coefficient (A) = 1.0; deposition coefficient (B) = 0.3; supersaturation with respect to ice, 10%; temperature, -83°C (190°K); pressure, 100 mbar. The relative mass growth rate is simply the growth rate per unit crystal mass.

order to develop conceptual models. Figure 22 shows the growth rate, relative growth rate, and terminal velocities for crystals over the size range of our measurements at 100 mbar and -80°C at 10% supersaturation with respect to ice. The saturation value selected here for computational purposes is arbitrary, and we are equally interested in evaporation (i.e., .4 could also be subsaturated). The 10% supersaturation value turns out to be the maximum that we can support from our observations and computations to be discussed subsequently. The growth rate computations follow *Fukuta and Walters* [1970] and the terminal velocities are Stokes law values. The relative growth rate is the fractional change of mass with time for individual crystals and indicates that the smallest crystals would double their mass in less than a minute, or likewise evaporate, for ± 10% changes from ice saturation while, crystals 50 μm in size would show little change over an hour. Recalling the cumulative mass distributions of Figure 16, it is important to recognize that 90% of the mass lies at sizes above 20 μm where terminal velocities are in excess of a few centimeter per second.

Terminal velocity computations can be applied to the size distribution measurements for flight 11 to generate the average mass flux and sedimentation rate at these flight levels. These results, shown in Figure 23, indicate a potential significant loss of mass at altitude in the absence of an updraft. With zero vertical velocity the bulk of the ice water mass can sediment a couple of kilometers without significant mass loss. Under appropriate conditions the great majority of ice water content can sediment to lower levels prior to evaporation. Clearly, since the ice crystal environment at a minimum is at ice saturation, the only way hydration can occur is to raise the temperature of the parcel by forced descent, by radiative heating, or by mixing with warmer air. One is left to conclude that the large ice water content that is elevated to the highest altitudes sediments and leaves the local vapor density essentially at ice saturation. At the coldest temperatures near cloud top, air entering the stratosphere should have a water vapor abundance simply that of ice saturation.

Further computations were performed for the ensemble growth rate and the necessary updraft to support ice saturation ratios above unity at the observation altitudes of flight 11 (see *Heymsfield and Sabin* [1989] for similar treatments in cirrus).

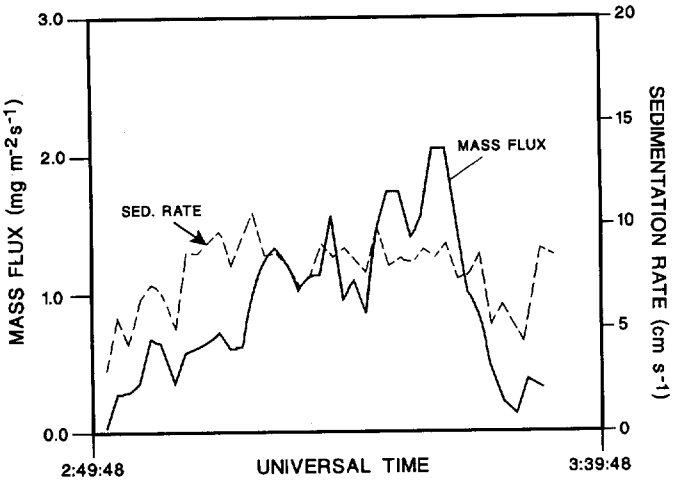

Fig. 23. Sedimentation rate and mass flux for flight 11 on February 4, 1987, flight data.

The results indicated that water saturation could not be produced at the measurement altitudes with reasonable updrafts in the presence of the observed competing ice crystals. Because the necessary updraft velocities are so high, it is necessary to examine the possibility of ice nucleation at much less than water saturation or possible ice nucleation at lower altitudes.

The high concentration of ice crystals spread through sizes from submicron to over 50 μm is difficult to reconcile with current knowledge of cirrus cloud development. During the last few years there have been several detailed studies of cirrus development at temperatures bridging -40°C [*Heymsfield and Sabin*, 1989; *Sassen and Dodd*, 1986]. Below -40°C, homogeneous nucleation of ice is extremely rapid and the observations support nucleation in a narrow temperature range centered near -40°C. Neither of the observers found liquid water below -40°C although isolated reports can be found in the literature (see *Rangno and Hobbs* [1986] for a review). At temperatures slightly above -40°C, water droplets are activated and freeze at slightly above water saturation, while at temperatures slightly below -40°C, solution droplets freeze before water saturation is reached (droplets unactivated). After the onset of ice nucleation, further ice nucleation ceases due to the rapid growth of ice crystals depleting the vapor supply. The excess vapor supplied by updrafts of ~ 1 m s^{-1} can only maintain slight supersaturations with respect to ice after ascents of a few hundred meters. (More recently, *Heymsfield and Miloshevich* [1993] have reported several meters per second updrafts in wave clouds producing ice crystal concentrations exceeding 100 cm^{-3} via homogeneous nucleation but still a relatively narrow range of altitudes for nucleation.)

The cloud scenarios documented by these workers are, however, vastly different and simpler than the top of a tropical cyclone. Their clouds were thin with bases just below the -40°C level and full vertical profiles and measurements could be performed with relative ease. The Australian data consist mainly of measurements near cloud top. Obviously, these measurements were also confined to the less vigorous cloud levels for safety reasons. The extremely long wet trajectory involves very complex microphysics embedded in very strong mesoscale convection. Cloud base is 100°C warmer and 10,000 times wetter than cloud top (see Table 1 for the relative range of vapor densities). Thus it is doubtful that a strong comparison can be drawn to stratified cirrus. In spite of the very high concentrations observed, the anvil tops observed here are, in reality, very tenuous with visual ranges of a kilometer being typical. Thus they are not at all optically dense and, as we will subsequently show, they are also optically thin in the infrared. In both cases this is a direct result of the small particle size.

The measurements on flight 11 near cloud top suggest that ice nucleation has been rampant if not recent. One can easily dismiss that the ice mass formed in situ at altitude: the observed ice water contents of 0.03 - 0.04 g m^{-3} are consistent with an adiabatic profile with an origin (altitude) only slightly above the -40°C level. While the bulk of ice water residing at the larger sizes may have arisen from much lower altitudes, the large numbers of small ice crystals were probably generated much nearer the levels of measurement. Is it possible to have new nucleation in the presence of existing ice crystals at altitude (-80°C)? To answer, one has to examine the available IFN at altitude, the necessary saturation ratio required for this nucleation, and whether dynamics exist to support it.

TABLE 1. Saturation Water Vapor Densities

Temperature, °C	Vapor Density With Respect to Water, ρ_w (g m^{-3})	Vapor Density With Respect to Ice, ρ_i (g m^{-3})	Saturation Ratio, ρ_w/ρ_i
0	4.844	4.844	1.000
-10	2.357	2.138	1.1022
-20	1.073	0.8830	1.215
-30	0.4533	0.3384	1.339
-40	0.1757	0.1192	1.474
-50	0.06171	0.03820	1.615
-60	0.01929	0.01098	1.756
-70	0.005247	0.002789	1.881
-80	0.001202	0.000614	1.96
-90	0.000221	0.000114	1.93
-100	0.000030	0.000018	1.71

The above values are from the Goff-Gratch formulation as published in the eighth revision, Smithsonian Meteorological Tables [*List*, 1984].

The necessary IFN has to first be a wettable CCN. In the work of *Heymsfield and Sabin* [1989] the CCN were of $(NH_4)_2SO_4$ chemistry and involved saturation ratios of 0.9 - 1.0 (with respect to water) at temperatures between -40° and -48°C, where they indicated ammonium sulfate deliquesces at relative humidities of 82%. The saturated solution is in equilibrium with water vapor at 82% relative humidity (R.H.) because of vapor pressure lowering. Thus it is only "wettable" at saturation ratios above 0.82 with respect to water (1.7 with respect to ice at -80°C). At -80°C, water saturation is nearly twice ice saturation and thus such nuclei still require 70% supersaturation with respect to ice for activation and ice nucleation. In terms of our problem the updraught velocities required to generate 100% supersaturation are about as easy as those required to generate 70% supersaturation. In short we need a CCN "wettable" at a much lower R.H.

The probability that a solution droplet homogeneously nucleates is related exponentially to its volume-free energy and directly to droplet size and time. As solution concentration increases, the volume free energy drops, decreasing the nucleation rate. The effect is directly related to the freezing point depression of bulk solutions. Thus with the vapor pressure lowering required for wetting at less than water saturation, comes a lowering of ice nucleation efficacy. Since both effects are colligative properties, a given percent reduction in vapor pressure lowering is accompanied by a proportional freezing point lowering. A ratio of $\approx 1.0\%\ \Delta P/1°\ \Delta T$ describes the essential result of interest. Thus a solution droplet of $(NH_4)_2SO_4$ in equilibrium at 90% R.H. at -50°C has a freezing point depression of $\approx$ 10° and would have the same probability of freezing as a pure water droplet of the same size at -40°C. At -85°C a hypothetical CCN with -45°C freezing point depression would again nucleate comparably to the pure water droplet at -40°C while requiring only 55% R.H. for equilibrium. Ammonium sulfate can be ruled out since it is not wettable below 82% R.H. The only likely available CCN is H_2SO_4. (Coincidentally, 55% R.H. is close to ice saturation.) Calculations of the necessary updraft to support new nucleation nearer to ice saturation have been made. Figure 24 shows the necessary updraft required to achieve 10% supersaturation with respect to ice and allowing H_2SO_4 to nucleate ice, while supporting growth of the ice crystal population observed for flight 11. While measured updraft velocities for flight 11 were quite low (the data from the low-resolution INS used on flight 11 are questionable) 1 m s^{-1} is easily achieved since updrafts exceeding 4 m s^{-1} were measured on flight 12 when the ER-2 passed over Jason's center. *Danielsen* [this issue] points out that while there was an absence of overshooting turrets and instead a general lifting of the tropopause, that there must be ubiquitous small-scale turbulence at cloud top mixing stratospheric air. This could provide a source of stratospheric H_2SO_4 CCN. The upper troposphere is the other most likely H_2SO_4 CCN source. Impactor measurements by NASA Ames personnel aboard the Convair 990 and DC-8 aircraft have shown H_2SO_4 CCN as the dominant aerosol in the upper troposphere (G. Ferry, personal communication, 1992). It is well known that H_2SO_4 nuclei in the upper troposphere and stratosphere are liquid and that the H_2SO_4 nuclei equilibrate to whatever water vapor abundance is provided. While our first choice of nuclei was not sulfuric acid, there is no known CCN other than sulfuric acid with the desired physical properties. Entrainment could introduce such nuclei

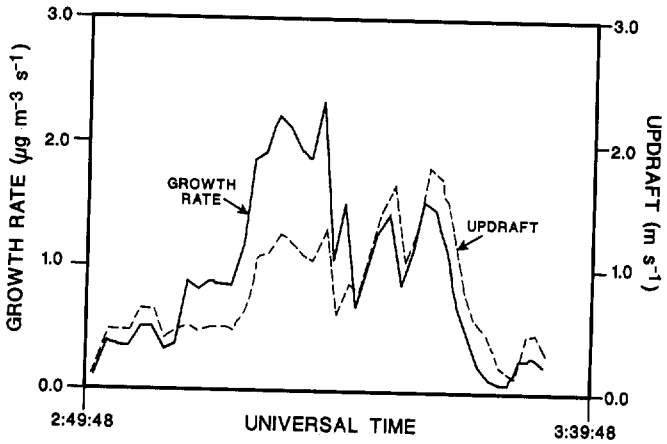

Fig. 24. Computed ensemble growth rate and updraft velocities required to support ice crystal growth at 10% ice supersaturation for flight 11.

resident in the upper troposphere into the clouds. Small-scale mixing with lower stratospheric air [*Danielsen*, this issue] could also provide a source of H_2SO_4 nuclei for the cloud. Given a tropical cyclone's extended lifetime, there should be sufficient opportunities for mixing. The authors believe H_2SO_4 CCN is a potential source for the IFN generating the high population of ice crystals observed.

In the absence of H_2SO_4 nuclei, one has to look at much lower altitudes for possible nucleation mechanisms operating closer to ice saturation with ammonium sulfate chemistry. One other region of possible high ice crystal nucleation is near -40°C where homogeneous nucleation first reaches significant rates. In the tropics this is near 12 km. As before, the problem with new nucleation at the midlevels in this cloud system is the potential competition from existing resident hydrometeors. The region near -40°C is undoubtedly fully glaciated and competition for water vapor may be strong, depending on the size distribution. Computations similar to that in Figure 24 can maintain levels near water saturation through significant altitudes only if updrafts are strong, CCN populations are deficient, and the ensemble growth rate of competing ice hydrometeors are unable to drive saturation values toward ice saturation. To some degree all three factors might be favorable here. *Marks and Houze*'s [1987] excellent Doppler radar study of Hurricane Alicia found the strongest updrafts (>8 m s^{-1}) at levels of 8-10 km (near -40°C at 25° N), while the model results of *Lord et al.* [1984] predict maximum updrafts in hurricanes at heights of 6-14 km. With regard to CCN populations any cloud level above cloud base would have to be deficient, having been drained of the most active CCN at cloud base. New IFN active at the -40°C level must arise from within the unactivated CCN that were unable to produce cloud droplets at cloud base. These are obviously smaller nuclei in terms of soluble mass and are rather poor CCN. However, CCN that become active IFN via homogeneous nucleation do not necessarily need to be good CCN. Heymsfield and Sabin's modeling shows that the greatest numbers of ice crystals are produced by CCN with masses of 10^{-13} to 10^{-15} g which were more likely to be present in abundance in their clouds as opposed to CCN of 10^{-12} g or larger mass. In the current situation, CCN with still smaller soluble masses are probably all that remains. Since it was observed here that nearly all CN become IFN, soluble masses near 10^{-18} g may even be utilized. This estimate is based upon a lower detectable CN limit of 10^{-17} g (0.015 μm) of which 10% is assumed soluble and is consistent with the notion that CCN are not simply that portion of total CN that are soluble but those with the largest soluble masses. The implication is that most CN have some soluble mass fraction. It is not necessary for there to be saturation values above water saturation, although it must approach it to activate the smallest masses overcoming the small droplet volume affording reduced nucleation opportunities. Homogeneous nucleation of ice would occur predominantly on unactivated CCN at values only slightly below water saturation. Our observations are consistent with the freezing of extremely small unactivated solution droplets (involving $(NH_4)_2SO_4$ or other soluble salts) since no large reservoir of unused CN exist at cloud top. The only alternative explanation is the loss of small CCN via scavenging.

With regard to competition from the resident ice hydrometeors, computations at 5-10 m s^{-1} updraught velocities reveal that this would only allow humidities near water saturation to exist if number densities were in the few per cubic centimeter range. The IWC could be quite high, 0.5-1.0 g m^{-3}, with still fewer but larger hydrometeors present. These hydrometeor number densities might be rather speculative, but typical maritime cloud base spectra show number densities of $\leq$100 cm^{-3}. After rising to 12 km, the concentration would be reduced to < 25 cm^{-3}. With coalescence and accretion very active, further reduction of hydrometeor concentrations by an order of magnitude seems quite plausible. Under any set of circumstances, cloud base number densities are too low to support a single level of new particle formation.

Ice nucleation would cease either after all IN are used or the generated ice crystals in combination with resident hydrometeors reduce vapor mixing ratios to ice saturation values. In such a scenario, ice nucleation may stretch over an altitude and temperature range much greater than the narrow 100 m and 2°C band found by *Heymsfield and Sabin* [1989]. Whether ice crystal spectra with the characteristics observed at -80°C can be produced after forming at -40°C and ascending 4-5 km, is an open question. It seems highly unlikely but greater in-depth knowledge of such a cloud system over a significantly larger vertical extent is needed to totally rule out.

The tops of tropical cumulonimbus anvils are regions of significant radiational cooling in spite of the low flux divergence. The greatly lessened air density offsets the effect of low-temperature radiative losses. Previously, *Griffith et al.* [1980] had measured cooling rates of 10° - 15°C per day in tropical cirrus. Following *Stephens*' [1978] work with water clouds, they were able to relate the effective cloud emissivity to ice water profiles (IWP = IWC · Z) derived from measured particle size distributions where

$$\text{Cloud Emissivity } (\epsilon_{cld}) = [1\text{-}e^{-K(\text{IWP})}] \qquad (1)$$

Here K is a broadband grey-body mass absorption coefficient (m^2 g^{-1}) and IWP is the integrated column ice water integrated from cloud top, or base, to the level in question. Values of K ranging from 0.076 to 0.096 were derived by *Griffith et al.* [1980] from in-cloud measurements. Later, *Starr and Cox* [1985] refined those values to a range of 0.054-0.069 by extrapolating the size measurements to include smaller unsized ice crystals. Recently, *Ackerman et al.* [1988] deduced a still lower value of 0.033 m^2 g^{-1} from size distributions of *Knollenberg et al.* [1982] over Panama. A closer look at (1) reveals that the K · (IWP) product is conserved in such calculations and errors in derived K values are compensated by offsetting errors in derived IWC. In our case, we have independent IWC measurements and have shown that we can accurately partition IWC among the ice crystal population. Furthermore, since K · (IWC) is simply the absorption cross section per unit volume, it can be computed directly using the particle size distributions and the complex refractive indices for ice.

A particle's absorption cross section (C_{abs}) is the product of its geometric cross section (Πr^2 for spheres) and the absorption efficiency factor (Q_{abs}). Details can be found in the work of *Van de Hulst* [1957]. Using the optical constants for ice from *Warren* [1984], Q_{abs} was computed for the wavelength range of 1-100 μm. The spectral variation of Q_{abs} λ for selected diameters is shown in Figure 25. The integrated values of Q_{abs} over the range of wavelengths associated with IR emission within the anvils (T=190°K) and the computed range of K are shown in Figure 26. The data in Figures 25 and 26 indicate that within the size range of our measurements, most of the ice crystals are grey (although highly colored) but

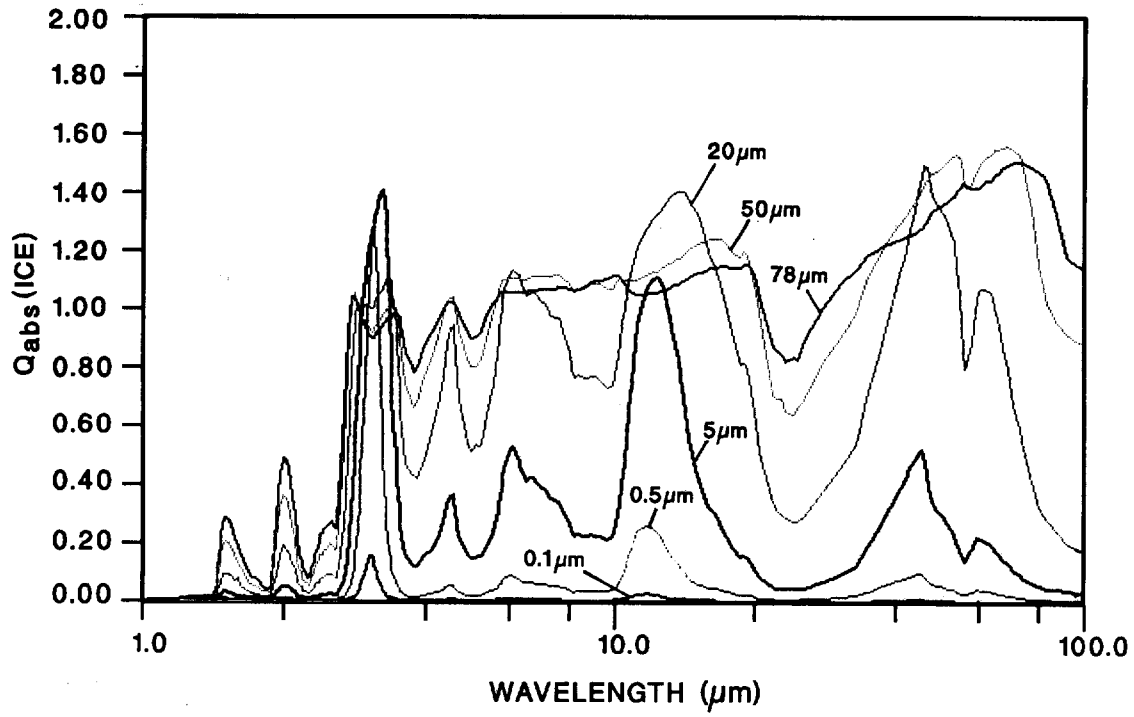

Fig. 25. The spectral variation of the absorption efficiency factor for ice spheres. Refractive index data are from *Warren* [1984]. Note that at small sizes the SNIR 3.0-μm band is the dominant feature and the increase in 1.5- and 2.0-μm absorption at larger sizes.

approach blackbody characteristics (high absorptance and emittance) at all sizes larger than the mean mass size (≈30 μm). The mass absorption coefficient becomes asymptotic at 0.095 for minimum sizes. Thus if all ice crystals were smaller than 10-μm diameter, maximum absorption/emission would be achieved by the available IWC. There is a corollary here in industry relating to the manufacture of pigments and ink toners to achieve greatest product efficiency where it is found that reduction of particle size below some upper limit no longer increases product efficiency. This size limit defines the threshold for the maximum absorption per unit mass of material and is of extreme practical importance. An examination of Figure 25 also reveals the potential for strong solar absorption at 3.0 μm with additional weaker regions at 1.5 and 2.0 μm. We will find these weaker bands of considerable interest when examining the sensitivity of cooling/heating calculations to particle size. For this cloud mass, one can assume that it is sufficiently thick to be viewed as a blackbody below all flight

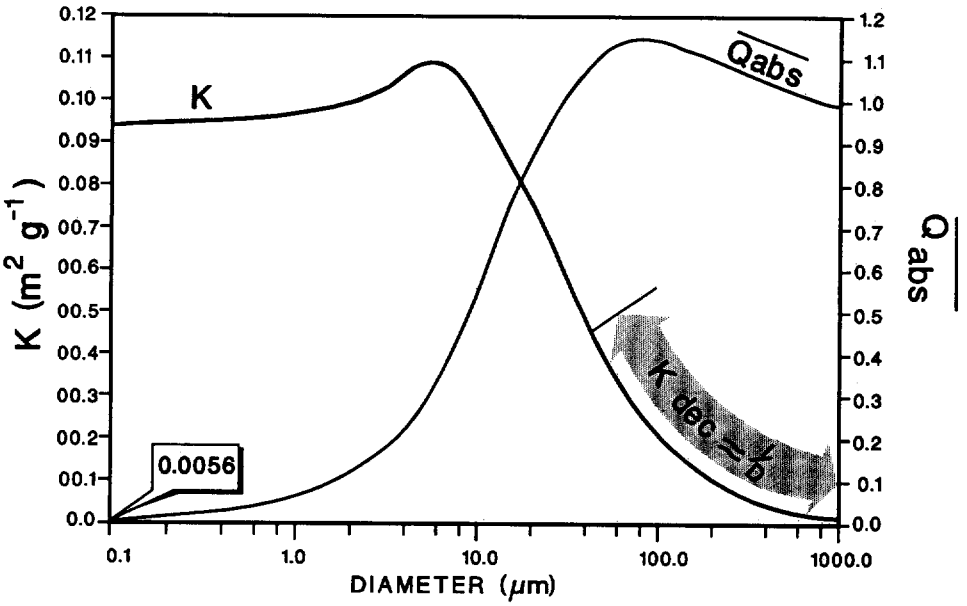

Fig. 26. Variation of absorption efficiency factor and mass absorption coefficient with ice sphere size. Computed values for K and Q_{abs} are weighted for absorption/emission of 190°K blackbody radiation.

levels of measurement. The emitted fluxes at level Z are assumed to arise at the temperature at level Z using the computed particle emittances ($\approx \epsilon\sigma T^4$). Radiational cooling computations thus require only the additional knowledge of downward irradiance at cloud top and downward effective emissivity for the cloud layer above level Z. For our purposes the downward irradiance at cloud top can be limited to two sources: solar near infrared (SNIR) and long-wave contributions from ozone at 9.6 μm. Stratospheric water vapor and CO_2 contributions are negligible. The ozone irradiance contribution was estimated from seasonally averaged data (0.3 cm of O_3) to be $\approx$ 0.07 mW cm^{-2}. (This value may be high since *Newell and Gould-Stewart* [1981] have suggested a reduction in ozone over the "stratospheric" fountain.) The SNIR heating contribution is of the same order but smaller than the radiational cooling at cloud top for most ice crystal sizes, and for the integrated size distributions as a whole, but not for all sizes, as we will see below. It is a maximum at local noon and, of course, zero at night. Since tropical cyclones last for days, its diurnal average is diminished, but since our flights were all during daylight hours, we have included an average daytime contribution equal to 0.6 times the SNIR maximum (0.6 is average cosine function for daylight hours at low latitudes).

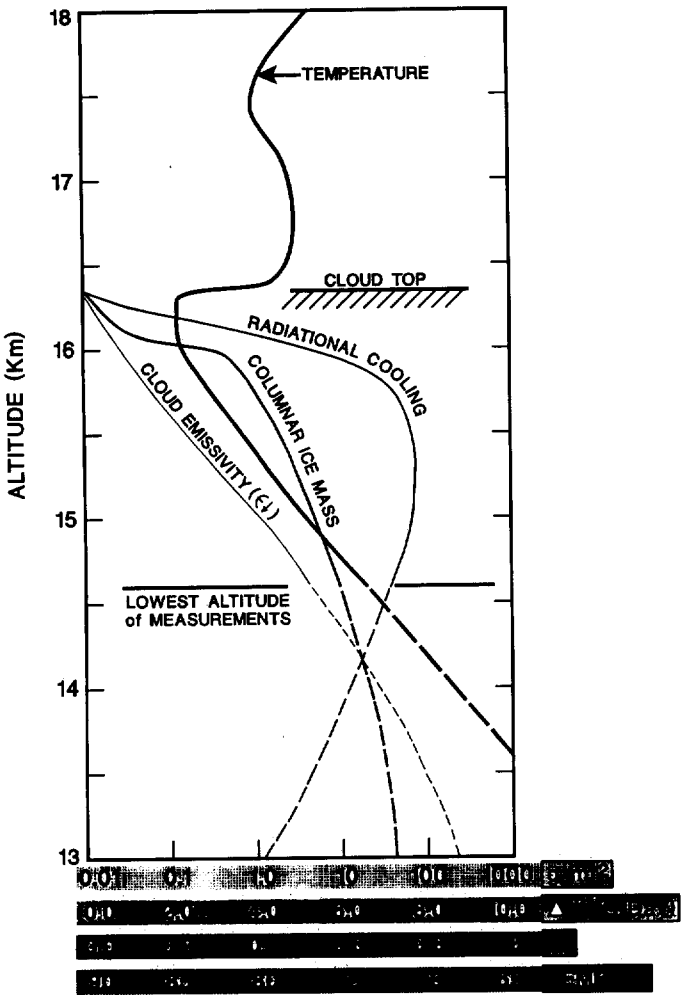

Fig. 27. Radiational cooling computed in anvil of flight 11. The radiational cooling computation was performed using complex refractive index of ice from *Warren* [1984] and the profiles of particle size distributions for the descent profile into the anvil of Damien (February 4, 1987), which was more uniform than the exiting profiles. Values below 14.6 km have been extrapolated.

The computational results are shown in Figure 27 for the IWP derived during descent. The downward flux emissivity $\epsilon_{\downarrow}$ and cooling rate indicate a more tenuous cloud than those reported by *Griffith et al.* [1980] who found flux emissivities approaching unity in a kilometer, while 2-3 km are required here. An entry profile closer to the tropical cyclone's center would have undoubtedly produced a higher emissivity quicker, as is evidenced by the more than doubling of IWC at 14.6 km nearer the center of the cloud pass and the lower radiative emission temperatures in Figure 13. The effect of our thinner cloud is reflected in a somewhat lower cooling rate but influencing a deeper layer. The derived values of K vary from 0.064 on entry to 0.036 at 14.6 km and are in good agreement with previously reported values. The cooling rate increases to $\approx$ 12°-15°C/d at night and is about 1/2 the value indicated at noon. Radiational cooling is probably not responsible for the pronounced inversion at cloud top, but it certainly could be contributing to its maintenance. It is also furthering the reduction of cloud top temperatures as a whole, particularly at night.

The rate of radiational divergence at cloud top and convergence at base was suggested by *Danielsen* [1982] as an important element in destabilizing the anvil and initiating turbulent mixing. However, the cooling profile of Figure 27 would tend to increase stability in the top kilometer or 2. The cloud top temperatures nearer the center of Damien in Figure 13 would indicate a greatly increased cloud opacity there and a cooling profile with maximum cooling closer to the cloud top, thus decreasing stability. As the anvil cloud moves away from the underlying cloud or the cloud system decays, the cirrus anvil is exposed to upwelling terrestrial radiation and rapidly heats as a layer. Cloud particle size sorting through differential sedimentation should tend to leave smaller crystals near cloud top and larger ones below, although our measurements revealed little difference in size distribution with altitude.

The smaller crystals turn out to be poor long-wave emitters/absorbers but are surprisingly effective in the SNIR. A 3-μm diameter, ice crystal has an absorption efficiency factor of $\approx$1.0 at the strong SNIR 3-μm absorption band but never exceeds 0.2 at wavelengths > 5μm. It is in fact possible to construct a set of daytime conditions in which the smaller crystals are heating while larger crystals (being nearly black at longer as well as shorter wavelengths) are cooling. Figure 28 shows the cumulative SNIR and emitted IR fluxes for selected ice crystal sizes observed near cloud top at 190°K and 0° zenith. Also shown are the SNIR absorptance and IR emittance for each size. It is evident that at only the larger sizes is the absorbed SNIR less than the emitted IR. Note also that for the larger crystals the 1.5-μm and 2.0-μm bands contribute more noticeably to the integrated SNIR totals. The ratio of the emitted IR to the absorbed SNIR shown in Figure 29 shows whether an individual particle is radiatively heating or cooling. The range of sizes that cool is shown to be restricted to $\approx$6-110μm. This rather surprising result can be explained rather simply. At small sizes (<6.0μm) absorption of 3.0μm SNIR is the dominant feature (Figure 25), and these particles heat. As ice crystal size increases, the 3.0-μm band saturates while the emission range of IR wavelengths (>5μm) approaches blackbody emittances. Now emission exceeds absorption resulting in a net cooling. As sizes further increase to above 110 μm, absorption at 1.5 and 2.0 μm (increasing directly with ice crystal volume) becomes sufficient to again result in an excess of SNIR heating.

Size-dependent radiative heating/cooling, as described here, could play a role in shaping the ice crystal distributions

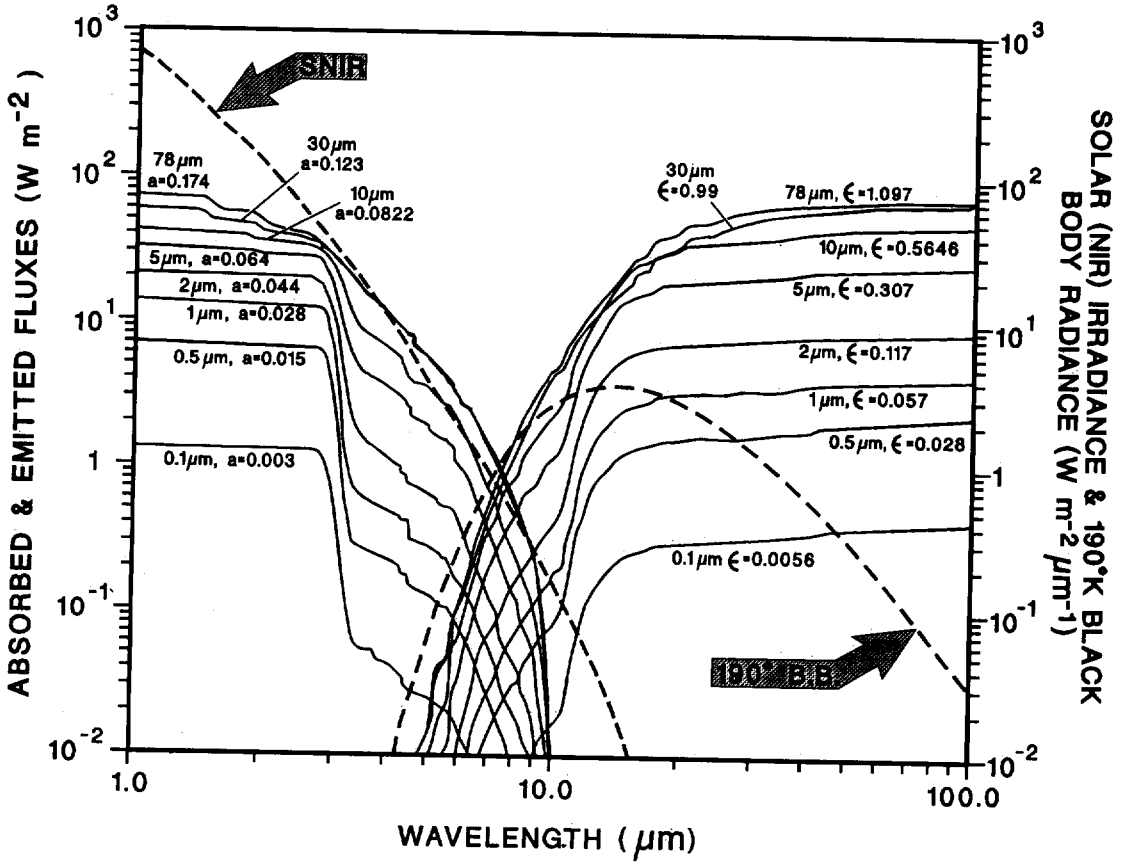

Fig. 28. Absorbed solar near-infrared and emitted infrared cumulative fluxes. The SNIR flux accumulates with decreasing wavelength while the emitted IR accumulates with increasing wavelength. The solar irradiance profile is from *Thekaekara and Drummond* [1971], and the blackbody curve absorptance values are shown for each spectral integration.

observed. Since a crystal being heated is at a higher temperature than one that is cooling, its vapor pressure is also higher. When saturation ratios are near equilibrium values, whether a crystal grows or evaporates may rest upon radiatively controlled particle temperatures. The induced temperature differences are proportional to crystal size. Thus in the current case, the larger ice crystals (>100 μm were not observed) may have been prevented from growing. The smaller set of particles being heated are capable of transferring the heat to the ambient air with greatly reduced impact on their growth but would still evaporate at ice saturation. Small crystals which are heating (but also growing) must transfer both latent and radiative loads by conduction to the ambient air. Large crystals which are cooling (growing) simply transfer

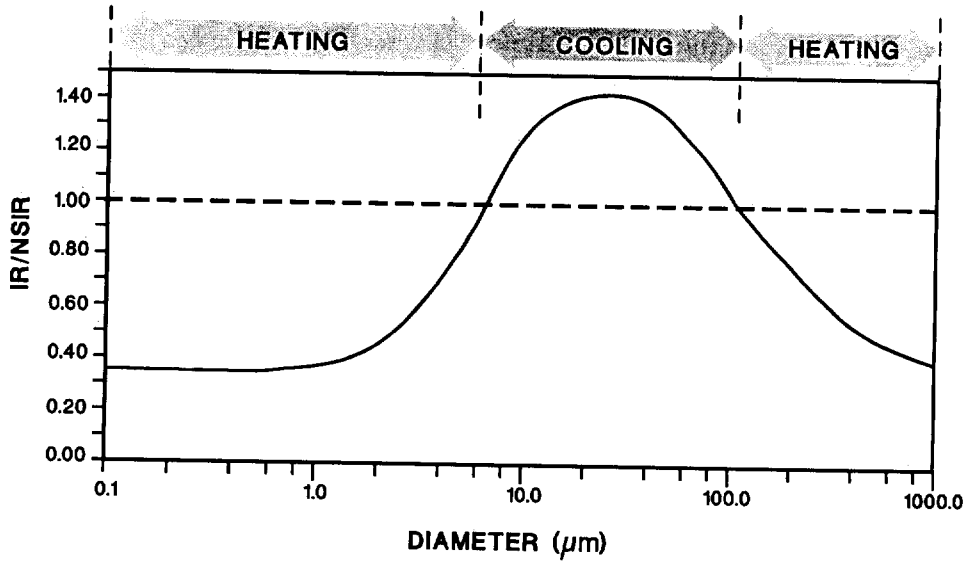

Fig. 29. Radiational heating/cooling as function of particle size. The size range for particles exhibiting radiational cooling are ≈6-110 μm. The particles <6 μm heat due to strong 3.0 μm absorption while particles >110 μm heat due to increasing absorption at 1.5 and 2.0 μm. Conditions are assumed to be at cloud top, 0° solar zenith, and 190°K.

their latent heat away radiatively. Radiation undoubtedly is the dominant component of diabatic heating processes at or near the cloud top. It is of greater magnitude than the latent transfer. The detailed exploration of the importance of these radiatively influenced microphysical processes is a suggested topic for future work. For the present, one must reexamine the notion that the high number density of small particles observed at cloud top are suggestive of recent nucleation: the observed size distribution may reflect a mass redistribution with sublimating small particles and growing midsized particles. Such a mechanism would support dehydration. *Danielsen* [this issue] suggests that it may, in fact, be an essential factor for dehydration above the tropical cyclone.

6. Conclusions

The following are a list of the major conclusions reached in this study:

On Microphysics

1. The observed number densities of ice crystals in the tops of cumulonimbus anvils are extremely high. Number densities range from 10 to 100 cm^{-3} in both tropical and continental regions. Homogeneous nucleation is required to explain the high number densities.

2. Water saturation is extremely unlikely to be produced at our measurement altitudes in the presence of the observed competing ice crystal population. Any new ice nucleation that occurs requires a CCN capable of deliquescing at low ice supersaturations. The ice forming nuclei responsible for the high ice crystal concentrations near the tropopause in tropical anvils are likely H_2SO_4 and of upper tropospheric or stratospheric origin.

3. There is strong evidence that mature tropical cyclones fully involve most CN in nucleation processes. Ice crystal number densities in active cloud regions correlate well with CN. In isolated tropical anvils and in continental anvil cirrus, a small fraction of total CN becomes involved.

4. Ice water contents in cumulonimbus anvils near the tropical tropopause can be quite high (approaching 0.1 g m^{-3}) and over 50X the vapor density.

5. The ice crystals in tropical cumulonimbus anvils associated with tropical cyclones over Micronesia were much smaller (<100 μm) than observed in tropical anvils over Panama in 1982 or in continental U.S. anvils in 1986 (up to 1 mm). The mean mass size is typically 20-40 μm. The ice crystals are quite dense and quasi spherical or of low aspect ratio.

6. Ice water contents for smaller ice crystals at very cold temperatures ($\approx$-80°C) can be derived accurately from a light scattering instrument calibrated assuming a response for ice spheres. Light scattering instruments can thus be used to derive accurate ice water contents when the crystals are small and amorphously spherical.

7. Ice water contents derived from two-dimensional Grey images of larger crystals provide reasonable estimates if proper choice of crystal thickness and bulk density can be made. Obviously, it is preferable to have independent IWC measurements as were available here.

On Hydration/Dehydration and Radiation Effects

8. The majority of the ice water mass observed in the tops of tropical cumulonimbus is condensed at lower altitudes and warmer temperatures and then transported to higher altitudes and colder temperatures. Because of the cold temperatures and ambient ice saturation the only way hydration can occur is to raise the temperature of the parcel by forced descent, by radiative heating, or by mixing with warmer stratospheric air. Thus the large ice water content elevated to the highest altitudes largely sediments and leaves the local vapor density at ice saturation.

9. Radiational cooling assists in cooling the cloud top. Solar near infrared may cause heating of both small and very large crystals even though the bulk of the ice crystal population is radiatively cooling. Such radiative effects would lead to a concentration of mass in 10- to 100-μm sizes accelerating sedimentation and assisting dehydration.

10. Ice crystal sorting at cloud top can lead to heating or cooling depending on the particle size and time of day. At night all sizes may be growing while during the day, growth occurs only at selected sizes.

Appendix: Detailed Description of Combined FSSP-Two-Dimensional/Optical System and Function

Refer to Figure A1 for detailed views of the optical system. The laser used was a 3.0 mW He-Ne TEM_{00} mode unit. The plane of polarization is rotated 45° with respect to the optical plane to minimize polarization sensitive reflections.

The 1-mm output laser beam was reshaped by a condensing lens set to generate a beam that was highly elliptical ($\approx$4 X 0.5 mm cross section) but collimated within the sample area. Near the forward end of the exiting optics tube, the laser beam is deviated 90^0 by a 45° mirror and passes between the tips of the optical extensions from the probe defining the sample area limits for the "in situ" measurements. The center of the sample area is the object plane for the primary objective. A second 45° mirror is located in the other tube which again deviates the laser beam by 90°, directing it and the light scattered from particles into the collecting optics.

The first element in the collecting optics is the 60-mm f.l. primary objective lens located approximately 40 mm from the second 45° mirror and provides a magnification of approximately 2.5X. The next several elements in the collecting optics are for the FSSP operation. The first (B-S1) is a semireflecting mirror which acts as a beam splitter to separate two-dimensional and FSSP activity. A smaller fraction of the laser beam and scattered light (~20%) reflects at a right angle where the light is collected by another 60-mm f.l. lens. A third lens of 45-mm f.l. is then used to focus the collected scattered light onto the photodiode detector pair. This lens also contains a dump spot to inhibit the transmitted laser beam from illuminating the photodiode detectors. Three 45° mirrors are employed to fold the collecting optics light path within the space available. At the image plane, a final 9-mm cube beam splitter is utilized to produce two scattered light images. The beam splitter is rotated 45° to neutralize polarization influences. That portion of the transmitted laser beam ($\approx$ 80%) and associated scattered light that transmits through beam splitter (B-S1) is reimaged by a 45-mm f.l. lens (LIS) onto the photodiode array for imaging by the two-dimensional instrument portion.

The FSSP used here differs from a standard FSSP in the manner in which the sample volume is defined. It uses the same sample volume definition scheme used on the Pioneer Venus particle size spectrometer probe [*Knollenberg and Gilland*, 1980] and on the FSSP-300 [described by *Baumgardner et al.*, 1992]. Briefly, the pulses of radiant energy produced by particles are

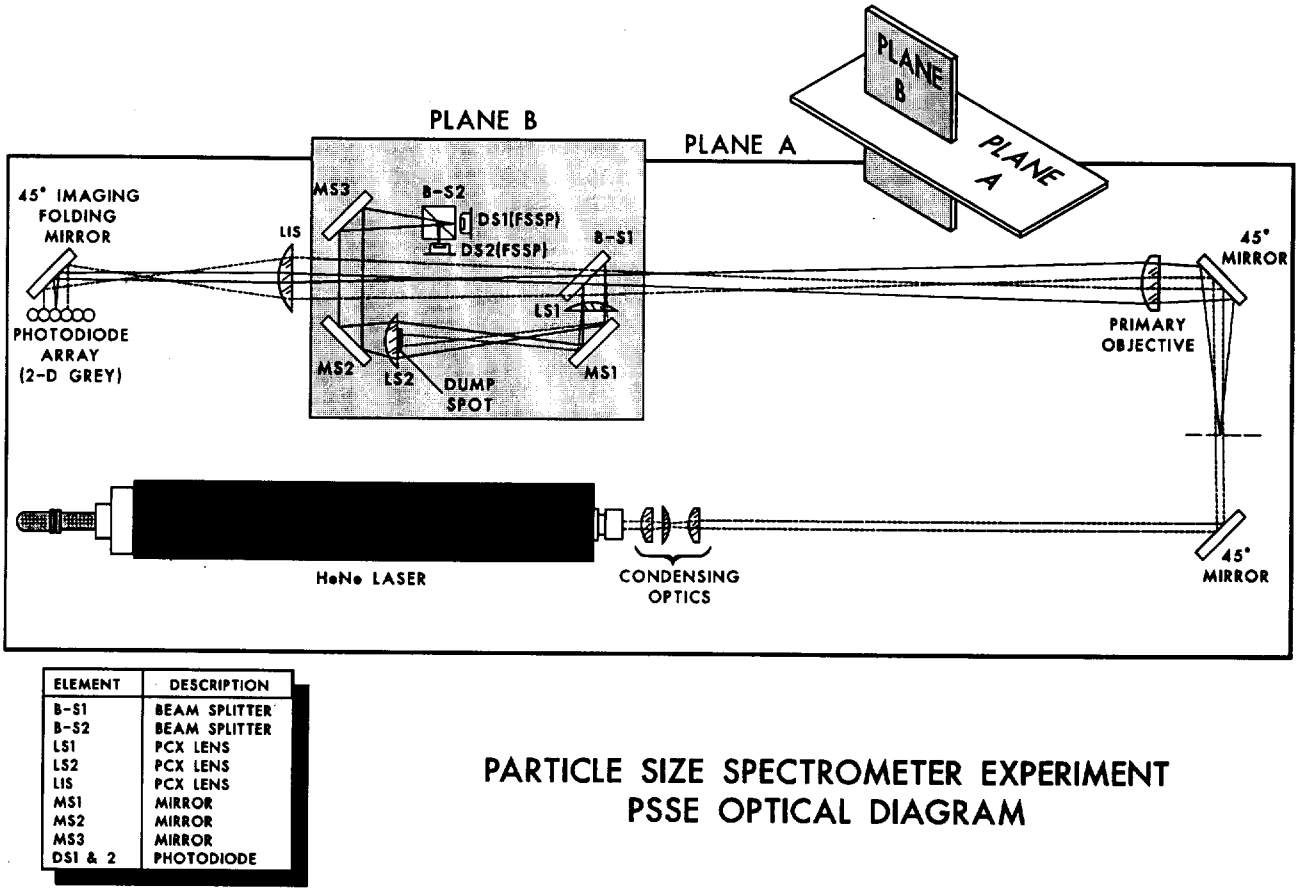

ELEMENT	DESCRIPTION
B-S1	BEAM SPLITTER
B-S2	BEAM SPLITTER
LS1	PCX LENS
LS2	PCX LENS
LIS	PCX LENS
MS1	MIRROR
MS2	MIRROR
MS3	MIRROR
DS1 & 2	PHOTODIODE

PARTICLE SIZE SPECTROMETER EXPERIMENT
PSSE OPTICAL DIAGRAM

Fig. A1. Optical system diagram for combined two-dimensional Grey and FSSP instrument.

sensed by photodiodes and read and compared by electronics within the DAS. One detector looks at all energy scattered into its collecting aperture and is the one that provides the sizing function. The other detector has its central horizontal diameter obstructed by a masked slit and therefore only receives significant energy from diffuse images that are out of focus or images from particle trajectories off-center. When the measured pulse heights of these two signals are compared, an acceptance criterion selects measurements within a limited sample area in the center of the laser beam. The actual size of this sample area is dependent upon the magnification of the imaging system, the size of the masked slit, and the gain ratio on the two detector circuits. The pulses from the unmasked detector are sized with a 16-channel pulse height analyzer in the DAS to determine particle size.

The optical functioning of the two-dimensional instrument portion is identical to that previously described [*Knollenberg*, 1982]. Sizing is by a direct relationship of particle-to-image size. The sample area is the product of depth-of-field and effective array width. The sample volume is the product of sample area and aircraft speed. The probe is controlled by the DAS and provides for sensing particles and storing the information for output to the DAS. Complete two-dimensional images of the particles are stored with four shades of grey. Depending on available recording capacity for storing images, the DAS determines whether full images or histograms produced by real-time image processing are recorded.

Acknowledgments. The authors wish to thank Rick Gallant and Joyce Mulcare of Particle Measuring Systems, Inc., for assisting with data analysis and preparation of the figures, respectively. The authors also wish to acknowledge the help of Marion Legg of NASA ARC for supplying Figure 13 and Ed Danielsen and Don Veal for many helpful discussions and review of the manuscript. Finally, a very diligent and thorough effort on the part of an unknown reviewer must be acknowledged.

REFERENCES

Ackerman, T. P., K. N. Liou, F. P. J. Valero, and L. Pfister, Heating rates in tropical anvils, *J. Atmos. Sci., 45*, 1606-1623, 1988.

Baumgardner, D., J. E. Dye, B. W. Gandrud and R. G. Knollenberg, Interpretation of measurements made by the FSSP-300 during the Airborne Arctic Stratospheric Expedition, *J. Geophys. Res., 97,* 8035-8046, 1992.

Danielsen, E. F., A dehydration mechanism for the stratosphere, *Geophys. Res. Lett., 9*, 605-608, 1982.

Danielsen, E. F., In situ evidence of rapid, vertical, irreversible transport of lower tropospheric air into the lower tropical stratosphere by convective cloud turrets and by larger-scale upwelling in tropical cyclones, *J. Geophys. Res.*, this issue.

Fukuta, N., and L. A. Walters, Kinetics of hydrometeor growth from a vapor-spherical model, *J. Atmos. Sci., 27*, 1160-1172, 1970.

Griffith, K. T., S. Cox, and R. G. Knollenberg, Infrared radiative properties of tropical cirrus clouds inferred from aircraft measurements, *J. Atmos. Sci., 37*, 1077-1087, 1980.

Heymsfield, A. J., Ice particles observed in a cirriform cloud at -83xC and implications for polar stratospheric clouds, *J. Atmos. Sci., 43,* 851-855, 1986.

Heymsfield, A. J., and R. G. Knollenberg, Properties of cirrus generating cells, *J. Atmos. Sci., 9*, 1358-1366, 1972.

Heymsfield, A. J., and Miloshevich, Homogeneous ice nucleation and supercooled liquid water in orographic wave clouds, *J. Atmos. Sci.*, in press, 1993.

Heymsfield, A. J., and R. M. Sabin, Cirrus crystal nucleation by homogeneous freezing of solution droplets, *J. Atmos. Sci., 46*, 2252-2264, 1989.

Kelly, K., Water vapor and cloud water measurements over Darwin during the STEP 1987 tropical mission, *J. Geophys. Res.*, this issue.

Kley, D., A. L. Schmeltekopf, K. Kelly, R. Winkler, T. L. Thompson, and M. McFarland, Transport of water vapor through the tropical tropopause, *Geophys. Res. Lett., 9*, 617-620, 1982.

Knollenberg, R. G., and J. R. Gilland, Pioneer Venus sounder probe particle Size spectrometer, *IEEE, Trans. Geoscu. Electron., GE18*, 1980.

Knollenberg, R. G., and D. Huffman, Measurements of the aerosol size distributions in the El-Chichon Cloud, *Geophys. Res. Lett., 10*, 1025-1028, 1983.

Knollenberg, R. G., A. J. Dascher, and D. Huffman, Measurements of the aerosol and ice crystal populations in tropical stratospheric cumulonimbus anvils, *Geophys. Res. Lett., 9*, 613-616, 1982.

Kritz, et al., Radon measurements in the lower tropical stratosphere: Evidence for rapid vertical transport and dehydration of tropospheric air, *J. Geophys. Res.*, this issue.

List, R. J., *Smithsonian Meteorological Tables*, 8th rev., p. 350, The Smithsonian Institute, Washington, D. C., 1984.

Lord, S. J., H. E. Willoughby and J. M. Piotrowicz, Role of parameterized ice-phase microphysics in an axisymmetric, non-hydrostatic tropical cyclone model, *J. Atmos. Sci., 41*, 2836-2848, 1984.

Marks, F. D., Jr. and R. A. Houze, Jr., Inner core structure of Hurricane Alicia from airborne doppler radar observations, *J. Atmos. Sci., 44*, 1296-1317, 1987.

Newell, R. J., and S. Gould-Stewart, A stratospheric fountain?, *J. Atmos. Sci., 38*, 2789-2796, 1981.

Rangno, A., and P. V. Hobbs, Deficits in ice particle concentrations in stratiform clouds with top temperatures <-30°C, Preprints, in *Conference on Cloud Physics*, pp. 20-23, American Meteorological Society, Boston, Mass., 1986.

Russell, P. B., L. Pfister, and H. B. Selkirk, The tropical experiment of the Stratosphere-Troposphere Exchange Project (STEP): Science objectives, operations, and summary findings, *J. Geophys. Res.*, this issue.

Sassen, K., and G. C. Dodd, Homogeneous nucleation rate for highly supercooled cirrus cloud droplets, *J. Atmos. Sci., 45*, 1357-1369, 1988.

Starr, D. O'C., and S. K. Cox, Cirrus clouds, I, A cirrus cloud model, *J. Atmos. Sci., 42*, 2663-2681, 1985.

Stephens, G. L., Radiation profiles in extended water clouds, II, Parameterization schemes, *J. Atmos. Sci., 35*, 2123-2132, 1978.

Stephens, G. L., The influence of radiative transfer on the mass and heat budgets of ice crystals falling in the atmosphere, *J. Atmos. Sci., 40*, 1729-1739, 1983.

Thekaekara, M. P., and A. J. Drummond, Standard values of the solar constants and its spectral components, *Nature, 229*, 6-9, 1971.

Van de Hulst, H. C., *Light Scattering by Small Particles*, Wiley, New York, 1957.

Warren, S. G., Optical constants of ice from the ultraviolet to the microwave, *Appl. Opt, 23*, 1206-1225, 1984.

K. Kelly, NOAA Aeronomy Laboratory, 325 S. Broadway, Boulder, CO 80303.

R. G. Knollenberg, Particle Measuring Systems, Incorporated, 1855 South 57 Court, Boulder, CO 80301.

J. C. Wilson, Department of Engineering, University of Denver, University Park, Denver, CO 80208.

(Received September 1, 1991;
revised October 5, 1992;
accepted October 16, 1992.)